Forced Changes in Modes of Variability in E3SM and CESM

John T. Fasullo[1], Julie M. Caron[1], Adam S. Phillips[1], Nicola Maher[2,3,4], Clara Deser[1],
Jiwoo Lee[5]
[1] NSF National Center for Atmospheric Research, Boulder, CO, 80301, USA
[2] Australian National University, Canberra, Australia
[3] Cooperative Institute for Research in Environmental Sciences, University of Colorado at Boulder, 80309 USA
[4]ARC Centre of Excellence for Weather of the 21st Century, Canberra, Australia
[5]Lawrence Livermore National Laboratory, Livermore, California

26 Feb 2026
Manuscript submitted to Journal of Climate

Corresponding author: John Fasullo, fasullo@ucar.edu

ABSTRACT: Modes of internal climate variability (MoV) occur on time scales of months to decades and are important drivers of climate anomalies, extremes, and impacts. While previous work has proposed changes in MoV in response to external forcing, traditional methods of diagnosing MoV are not well-suited for separating internal and forced variations. Moreover, the robustness of simulated changes to model structure, and particularly to resolution, remains largely untested. In this work, we use an updated climate variability diagnostics package, multiple standard-resolution (SR) climate model large ensembles, and a recently released high-resolution (HR) climate model ensemble to assess model fidelity and simulated changes in MoV from 1920 to 2100. The sensitivity of traditional MoV definitions to aliasing of mean-state responses to external forcing is illustrated, highlighting the opportunity provided by large ensembles in their separation. The model dependence of MoV changes, once forced mean-state responses have been removed, is demonstrated, indicating a lack of robustness in several previously proposed responses. While simulation of MoV is not found to improve systematically in the HR ensemble relative to the SR ensemble, differences in MoV and their responses to forcing are identified, highlighting a potential caveat for conclusions based solely on SR model consensus.

SIGNIFICANCE STATEMENT: Modes of climate variability (MoV) are a key consideration in both Earth system detection and attribution efforts and in projections of associated impacts. Moreover the MoV themselves may exhibit forced changes and influence the magnitude and frequency of extremes. However, traditional MoV indices may alias mean-state changes, leading to erroneous conclusions. This work estimates forced changes in MoV after removing evolving background changes in the mean-state in four modern climate model large ensembles and a recently produced high-resolution model ensemble and its standard-resolution counterpart. The analysis assesses inter-model consistency in depicting forced changes in the MoV and the dependence of responses on resolution. Our findings identify a strong model dependence of simulated changes as a result of structural uncertainty, specifically highlighting the role of model resolution, underscoring the uncertainty of future changes.

KEYWORDS: Climate variability, climate modeling, internal variability, climate change, high-resolution modeling.

1. Introduction

Modes of internal climate variability (MoV) can drive impacts, confound diagnoses of anthropogenic climate change, and impart predictability on seasonal to multidecadal timescales [Liu and DiLorenzo 2018, Cai et al. 2020, Van Oldenborogh et al. 2021, Power et al. 2021, Wang et al. 2023, McGregor 2024]. MoV are also a key modulator of climate-driven impacts [Vázquez et al. 2017, Liu and DiLorenzo 2018, He and Li 2019, McPhaden et al. 2020, Cai et al. 2021, Power et al. 2021] and impact projections focusing only on mean state changes, rather than changes in variability, often understate damages due to nonlinear responses in socioeconomic, biological, and ecological systems [Thornton et al. 2014, Vázquez et al. 2017, Beobide-Arsuaga et al. 2025].

Interpreting observed climate fluctuations and tracking climate responses to external forcing agents (i.e. the “forced response” or FR) depends on the successful separation of externally-forced and internally-driven variability [Dai et al. 2016, Deser et al. 2017, Iles and Hegerl, 2017, Hu et al 2024, Liang et al. 2024, Guinaldo et al. 2025]. In addition, internal modes themselves may be affected by external forcing, though mode indices, which have traditionally been defined for historical climate, can themselves be susceptible to aliasing of base-state climate responses [Deser and Phillips 2021]. Diagnosing and projecting internal modes in a changing climate is therefore both extremely important and a considerable challenge.

Shifts in internal modes can take several forms. These include shifts in mode seasonality, magnitude, spatial structure, and teleconnections [Fasullo et al. 2018, Fogt and Marshall 2020, Haszpra et al. 2020, Yang et al. 2021, Zheng et al. 2021, Sun et al. 2022, O’Brien and Deser, 2023, Kim et al. 2024]. The temporal structure of responses can also be complex and non-monotonic, and external forcing can alter the regional expression of dominant eigenmodes [Kostov et al. 2017, Ji et al. 2024]. Changes in the El Niño / Southern Oscillation (ENSO) have received particular attention, with the duration and shifts between its phases being central to climate impacts [Wang et al. 2023, Jia et al. 2025]. In some instances, these MoV responses can result from shifts in base-state climate that affect the processes underpinning the modes themselves [Son and Lee 2006, Branstator and Selten, 2009, Wang et al. 2017, He and Li 2019, Seager et al. 2019]. Interactions between modes have also been identified as a source of change and these include the influences of the NAO on AMOC [Delworth and Zeng, 2016, Delworth et al. 2016], the NPO on ENSO [Chen et al. 2024], and the mutual coupling between ENSO, the North Pacific Meridional Mode (NPMM), and the IOD [Amaya 2019, Polonsky and Torbinsky 2021, Stuecker et al. 2025]. Thus a FR in one mode can cascade to others, and these links can be driven by either coupled processes or processes that are internal to a single component of the Earth system [Seager et al. 2019; O'Brien and Deser, 2023].

Our understanding of MoV changes is hampered by the uncertainties that exist in detecting and quantifying responses of modes to external forcing. Chief amongst these uncertainties are structural model uncertainty and observational uncertainty [Arias et al. 2021, DiLorenzo et al. 2023]. In observational studies, the susceptibility of traditional MoV indices to base-state changes is often not considered, leading to their potential conflation. In model-based studies, it is rare to examine the robustness of changes in MoV across multiple models while separating forced and internal components of variability. Confidence in simulated changes can be increased by skill-based culling of ensembles [Knutti et al. 2017, Lee et al. 2021, Wang et al. 2024] but this too can be undermined, even in cases of model consensus, by lack of physical understanding and systematic model bias [Woollings et al. 2018, Amaya 2019]. Studies using only a single model or few ensemble members with multiple models are particularly vulnerable [Cai et al. 2015, Ng et al. 2018] and studies using high-resolution ensembles have yet to be performed, though early results suggest an influence on the coupled processes relevant to multiple modes [Wengel et al. 2021, Wills et al. 2024].

In this work, the challenges of understanding MoV and their responses under climate change are considered through the use of 6 selected climate model ensembles. These ensembles include four large ensembles (≥20 members each) and a recently released high-resolution ensemble along with its standard-resolution counterpart, each of which consists of 10 members. These ensembles are unique resources that allow for benchmarking models, estimating FRs, and separating forced and internal variability [Maher et al. 2018, Deser et al. 2020, Fasullo et al. 2020, Fasullo et al. 2024, Maher et al. 2025]. Our analysis also makes use of an updated climate variability diagnostics package (Maher et al. 2025) to benchmark models and evaluate simulated changes relative to pre-industrial (piC) conditions for past (1920-1980), present (1980-2040), and future (2040-2100). Details about the model ensembles, diagnostics package, and datasets used are presented in Section 2, along with additional background motivation. The character of interannual climate variability and its projected changes in the 6 model ensembles are examined in Section 3. A focus is then given to specific modes, with Section 4 providing an assessment of ENSO, Section 5 addressing projected changes in modes closely tied to ENSO, and Section 6 addressing changes in other extratropical modes. A summary and discussion of results and their implications is presented in Section 7.

2. Materials and Methods

a. The Exascale and Energy Earth System Model versions 1 and 2

The Energy Exascale Earth System Model (E3SM) is a fully coupled Earth system model developed and supported by the U.S. Department of Energy (DoE) [Golaz et al. 2019, 2022], with the goal of addressing challenges in projecting Earth system variability relevant to the energy sector. In both E3SM versions 1 (E3SM1) and 2 (E3SM2) the model resolution is nominally 1° for all model components with 72 vertical levels in the atmosphere. Equilibrium climate sensitivity is estimated at 5.3K in E3SM1 and 4.0 K in E3SM2. To aid in the diagnosis of MoV and climate change, large ensembles (LEs) have been produced with both E3SM1 (Stevenson et al. 2023) and E3SM2 (Fasullo et al. 2024), consisting of approximately 20 members each. Both ensembles use initial conditions that sample a broad range of initial oceanic climate states (so-called “macro” initialization) and simulate transient climate from 1850 to 2100. External forcings differ between the ensembles, with the E3SM1-LE using the CMIP5 historical and high-forcing future scenario RCP8.5 provided by the Coupled Model Intercomparison Project Phase 5 (CMIP5, Forster et al. 2013, Meinshausen et al., 2011), while the E3SM2-LE uses historical SSP3-7.0 forcing protocols provided by the Coupled Model Intercomparison Project Phase 6 (CMIP6, Eyring et al., 2016). In CMIP6, an issue arising from inhomogeneities in data sources for biomass burning aerosol emissions has been identified (Fasullo et al. 2022, Fasullo et al. 2024). As smoothed biomass burning emissions simulations are not available through 2100 for E3SM versions, the CMIP6 forced CESM2, E3SM1 and E3SM2 ensembles are used for the late 21st century, when the impact of smoothed historical emissions is negligible. Other inconsistencies between CMIP5 and CMIP6 scenario forcings are known to exist, even for the historical era, and these exist as a caveat in discussing inter-ensemble contrasts (Fyfe et al., 2021, Holland et al. 2024).

b. *The Community Earth System Model versions 1 and 2*

The Community Earth System Model (CESM) is a state-of-the-art, fully-coupled climate and Earth system model developed through collaboration among research institutions, led by the National Center for Atmospheric Research and funded by the National Science Foundation and the Department of Energy. The model resolution is nominally 1° for all model components with approximately 30 vertical levels in the atmosphere. Equilibrium climate sensitivity is estimated at 4.1K in CESM version 1 (CESM1) and 5.3 K in CESM version 2 (CESM2) (Gettelman et al. 2019). A 40-member LE has been produced using CESM1 (Kay et al. 2015) and two 50-member LEs have been produced using CESM2, one with CMIP6 forcing and one using smoothed biomass burning emissions (Rodgers et al. 2021, Fasullo et al. 2022). For the reasons stated above regarding the E3SM2-LE, the smoothed biomass burning emissions members are used herein. The CESM1-LE uses a start date of 1920 in all but one member and a micro initialization strategy, whereby a single ocean state and small differences in atmospheric temperature are prescribed to generate ensemble spread. In contrast, CESM2-LE uses a strategic combination of micro- and macro-initialization in 1850 to address the sensitivity of ensemble spread to the method of initialization (Deser et al., 2024). Prescribed external climate forcings also differ between the ensembles with the CESM1-LE using the CMIP5 historical and RCP8.5 forcing protocols and the CESM2-LE using the CMIP6 historical and SSP3-7.0 forcing protocols.

A high-resolution ensemble using CESM version 1.3 has also recently been produced and released to the community, referred to herein as CESM1HR (Chang et al. 2020, 2025). The ensemble consists of a single member extending from 1850 to 2100 under CMIP5 historical and RCP85 forcing protocols and initialized in 1850 from a 500 year preindustrial simulation, resulting in minimal drift, and 9 additional members initialized from this member in 1920 and extending to 2100 with the same forcings. Unlike the CESM1-LE and CESM2-LE, CESM1HR uses a spectral element dynamical core. This ensemble employs the micro-initialization approach used in the CESM1-LE. The CESM1HR model has 0.25° atmosphere/land and 0.1° ocean/sea ice components that resolve mesoscale atmospheric, land surface, and oceanic processes, including tropical cyclones, mountain topography, and oceanic eddies, to better resolve physical processes that rely on parameterizations in standard resolution climate models. Increased resolution also better resolves topography and bathymetry and has been shown to better represent coupled atmosphere-ocean interactions (Chang et al. 2020, Wengel et al. 2021, Wills et al. 2024). Its impact on the fidelity of MoV simulation is however largely unknown and this is therefore an important science question being explored here. To isolate the effect of resolution, a standard resolution nominal 1° 10-member companion ensemble with minimal parameterization changes, referred to as CESM1SR, has been generated using the same model configuration, including its spectral element dynamical core.

c. The Climate Variability Diagnostics Package version 6

The Climate Variability Diagnostics Package version 6 (CVDPv6) produces diagnostics of MoV, long-term trends and climatologies in both models and observations (Maher et al. 2025). A key feature of the package is its ability to account for forced signals using various approaches including removal of: 1) a linear trend, 2) a 30-year running mean (an approach often used for Niño3.4 SST), or 3) a least-squares quadratic fit. Additionally, the option also exists to remove the ensemble mean (EM) when large ensembles are used, which provides a more accurate means of accounting for the FR.

In this work, we focus on the dominant MoV including ENSO (diagnosed from Niño3.4 SST per Deser et al. 2012), Pacific Decadal Variability (PDV, diagnosed from the leading Empirical orthogonal functions (EOFs) of NP SST per Mantua et al. 1997 and Deser et al. 2010), the Indian Ocean Dipole (IOD, diagnosed from the anomalous SST gradient per Saji et al. 1999), and the NPMM (Chiang et al., 2004). Extratropical modes are also assessed such as the Southern Annular Mode (SAM, diagnosed from Thompson and Wallace 2000), Atlantic Multidecadal Variability (AMV, Deser and Phillips 2021), the Pacific / North American mode (PNA, Hurrell and Deser, 2010), and North Atlantic Oscillation (NAO, Hurrell and Deser, 2010).

To illustrate the susceptibility of traditional MoV diagnoses to forced mean-state changes, the evolution of select modes are shown in Figure 1 for CVDPv6 analyses spanning 1920 to 2050 in which the underlying EM is either retained (wEM) or removed (rmEM). For the modes shown, both the mode patterns and indices alias forced mean-state change if the EM is not first removed. This is evident in the NAO, for example, where stronger patterns and transient changes are simulated for all LEs under the wEM approach relative to the rmEM approach, where no significant changes over time are diagnosed (Fig. 1a-c). Similarly, for the SAM, stronger patterns and changes over time are reported in the wEM case in all ensembles, whereas no significant index changes are reported for the rmEM case (Fig. 1d-f). For the PNA (Fig. 1g-i), EM aliasing is again evident, but with a character that is both model dependent and variable in time. Index trends in the rmEM case are again negligible (Fig. 1i). Impacts of forced change on these modes with respect to both mode patterns and time evolution are significant in both the historical era and the early to mid-21st century, suggesting that current diagnoses are likely to be aliasing base state changes in the present day if the MoV are not properly defined. Moreover, the changes in some modes are non-monotonic, highlighting the challenge of accounting for the EM in historical-era observations and the potential limitations of linear detrending. Differences in the computed mode patterns between the wEM and rmEM cases (Figure S1) reveal that forced mean-state changes in the Azores High, Southern Hemisphere (SH) storm track, and Aleutian Low alias onto the NAO, SAM, and PNA, respectively.

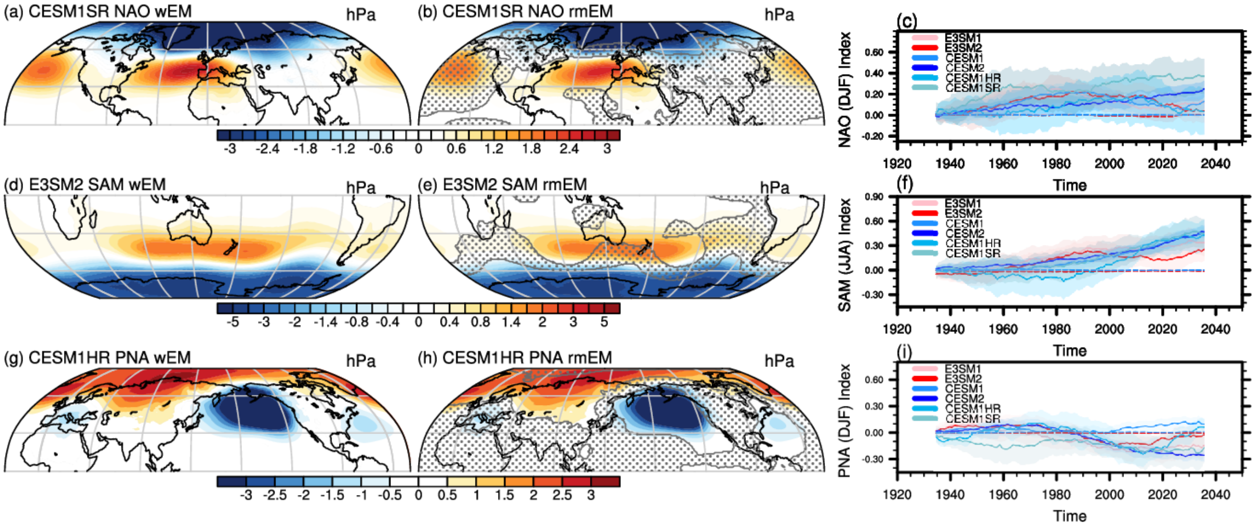

Figure 1: Simulated changes in select MoV over the period 1920-2050 when the forced mean-state response is (wEM, left column) and is not (rmEM, center column) included, and their corresponding index timeseries (wEM solid, rmEM dashed) (right column). Modes shown are the NAO in Dec. through Feb. (DJF, top), the SAM in June through Aug (JJA, middle), and the PNA in DJF (bottom). Stippling in the center column denotes regions where the trend differences between left and center column are not significant (i.e. < 2-standard error range). Shading on the index time series denotes the 2-standard error ranges of the ensemble spreads in 30-year running means.

To assess model simulation of MoV across timescales, we apply the CVDPv6 to a variety of time intervals in both the piC and historical simulations. These include an analysis of the “past”, “present”, and “future”, as defined above, and multiple equal length (i.e. 60-year) segments from the piC. Simulated patterns from the piC and changes across these respective time periods with ensemble means removed are the focus of this analysis. In addition, an observational benchmarking case is performed to assess model fidelity. This case compares the ensembles to ERA5 from 1950 to 2023 for all fields except precipitation, in which case a comparison to GPCP CDR is conducted from 1979 to 2023. This case uses linear detrending for modes defined using sea level pressure and removal of 30-year running means for other modes, motivated by results described below.

d. Observations

To evaluate model skill, multiple observation-based datasets are used. These include outputs of near-surface air temperature (T_{2m}) and sea level pressure from the European Centre for Medium Range Weather Forecasts (ECMWF) Reanalysis Version 5 (ERA5; Hersbach et al., 2019). ERA5 is the successor to ERA-Interim (Dee et al. 2011), increasing the resolution of reported fields, the range of fields assimilated from satellite instruments, and the simulation accuracy as compared against a broad range of observations. For evaluation of precipitation fields, retrievals are used from the Global Precipitation Climatology Project (GPCP) Climate Data Record (Adler et al., 2020). This improved version takes advantage of refined rain gauge estimates used for calibration and indirect precipitation estimation from top-of-atmosphere longwave radiances.

e. Statistical Methods

Statistical significance is assessed generally under the assumption that model biases and inter-model contrasts are gaussian. For model evaluation, observation-simulated differences exceeding the two-standard deviation (2σ) range are deemed meaningful. For model inter-comparisons, the two-standard error range of the ensembles is used, with significant differences being identified where those ranges fail to overlap. Pattern correlations are estimated from the area-weighted Pearson product-moment coefficient of linear correlation.

3. Climate Variability and Its Changes

The mean spatial patterns of the interannual standard deviation (σ) of T_{2m} across the four time periods and six ensembles used are shown in Figure 2. The patterns in the piC climate, shown in the left column, are characterized by large values at high latitudes and over land, with minima in the tropical Indo-Pacific region. A key region of inter-model disagreement in the piC pattern exists in the eastern equatorial Pacific, which will be shown to be consistent with contrasts in ENSO strength below. Agreement with ERA5 based on the observational benchmarking CVDPv6 case from 1920-2023 is strong, with pattern correlations (PCs) at or above 0.87 for all ensembles. Differences in PCs across ensembles (i.e. model difference) are on the same order of magnitude as the 2σ range within each ensemble (~0.02; i.e. internal climate variability), and thus inter-ensemble differences in PCs against observations are not meaningful. Generally, all ensembles overestimate variability in the tropical Indo-Pacific region (hatching), and underestimate variability in tropical and some subtropical land regions (stippling). Increasing resolution in CESM1HR has the effect of reducing variability across most of the globe (stippling in Fig. 2u), with the exception of isolated regions such as the subtropical Pacific Ocean (hatching).

Mean simulated changes in the ensembles from the piC to the past are generally weak (second column from left), with the strongest and most statistically significant changes simulated in CESM1HR (Fig. 2r). In the present (second column from right), increases in simulated variability are detectable in the central and eastern equatorial Pacific Ocean in all ensembles. Decreases in variability are simulated in the Southern Ocean in all models, with the strongest reductions simulated by CESM1HR. In the future, detectable changes in variability are widespread in all ensembles, with increases simulated generally across the tropics and subtropics, particularly over land, and decreases simulated in the Southern and Arctic Oceans. There is a strong seasonality to simulated decreases, with land regions prone to snow cover and ocean regions prone to sea ice in the present day exhibiting the largest decreases, typically in winter (DJF for NH, and JJA for SH, right columns of Figs. S2, S3) Notable inter-model contrasts include a lack of significant future increases in both CESM2 and CESM1HR in much of the equatorial Pacific Ocean.

Simulated changes, which are not generally related to a model's mean state representation (Suarez-Gutierrez and Maher, 2026), act generally to reduce the spatial gradients in variability, particularly for the future where PCs of changes with piC patterns are strongly negative in all ensembles (<-0.6). This weakening is driven by a general tendency toward increased variability at low latitudes and decreases in the extratropics, with the previously noted exceptions. More than half of land regions exhibit a statistically significant change in variability in the future in all ensembles, with simulated reductions dominating high latitudes and increases being pervasive in tropical and subtropical land regions (right column). The effect of increasing resolution in CESM1HR is to augment increases in variability from the piC to the past and present, and to decrease them from the present to the future, particularly in the equatorial Pacific Ocean. Decreases in variability in the Southern Ocean are also detectably stronger in CESM1HR compared to CESM1SR in all time periods.

To assess relative consistency across simulated patterns, a multi-ensemble mean (MEM) is constructed, consisting of the mean across ensembles of the future change patterns in the right column of Fig. 2. Each ensemble-mean pattern is then correlated against the MEM. The pattern of future change in CESM1HR exhibits the lowest PC of all the ensembles at 0.73, versus a range of 0.84 to 0.92 for the other ensembles, suggesting that simulated changes are somewhat distinct from the other ensembles due to model resolution (Table S1).

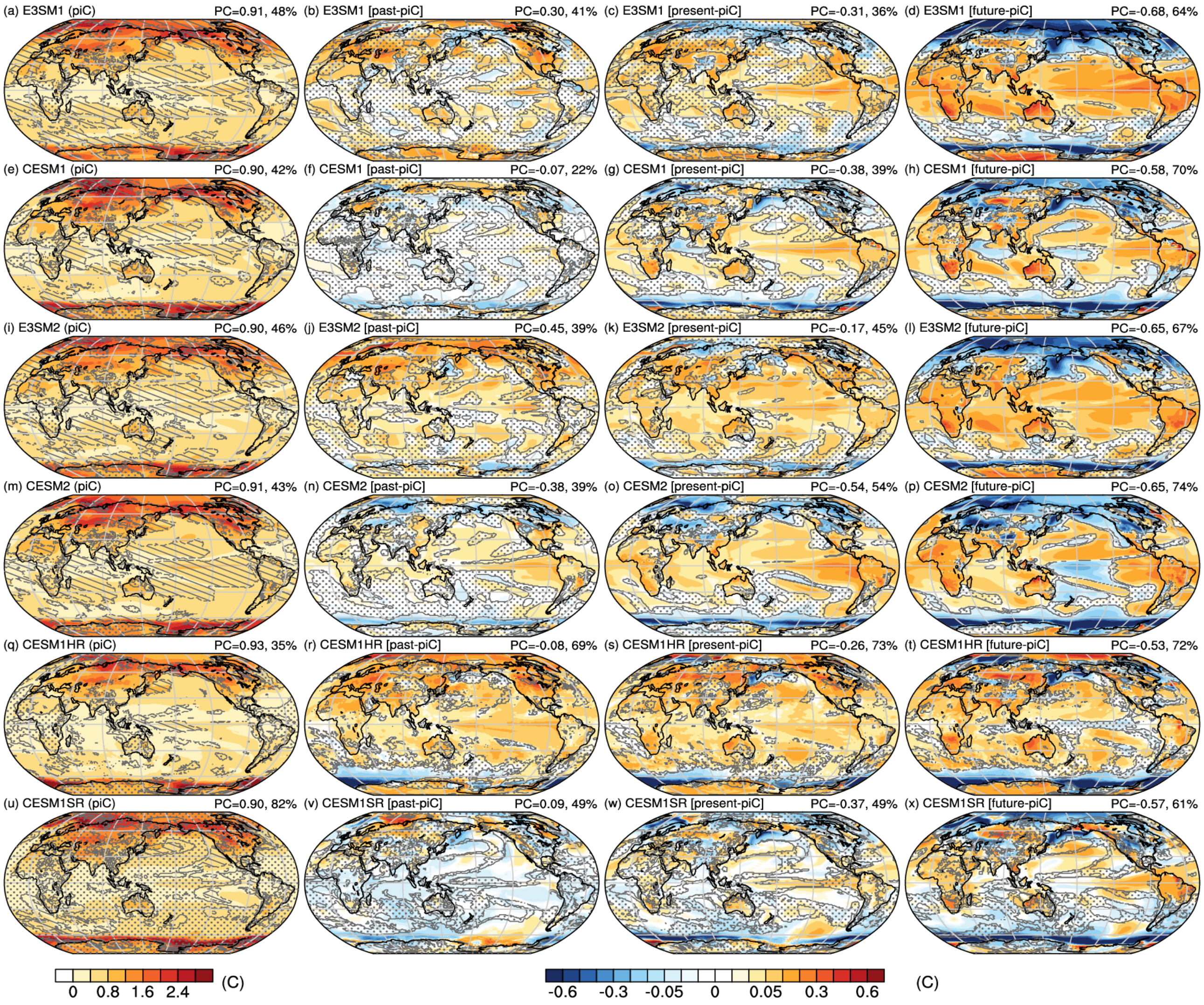

Figure 2: Standard deviation of annual mean T_{2m} (K) for the piC (left column), and its EM differences from the piC for past (1920-1980, left-center column), present (1980-2040, right-center column), and future (2040-2100, right column). Models shown include E3SM1 (a-d), CESM1, (e-h), E3SM2 (i-l), CESM2 (m-p), CESM1HR (q-t), and CESM1SR (u-x). Values in the headers indicate the mean pattern correlation (PC) against observations for 1920-2023 and the percent of the globe with significant bias (left column) or land regions with significant change (other columns). Regions are stippled (hatched) where observations lie above (below) the ensemble range (left column) or stippled where differences with the piC are not significant. In the bottom row, in contrast to other rows, stippling (hatching) indicates regions where differences between CESM1SR and CESM1HR are significant and positive (negative).

The spatial patterns of the interannual σ of precipitation (P) across the four time periods and the six ensembles used are shown in Figure 3. The mean patterns during the piC for all ensembles are characterized by large values in the Inter-Tropical Convergence Zone (ITCZ) and low values in the subtropics and high latitudes. Generally, these patterns correlate strongly to mean precipitation patterns, suggesting variability proportionate to the mean, with the main contrasts across ensembles relating to the intensity and extent of the ITCZ.

Ensemble-mean PCs against observations exhibit a greater spread between models for P than for T_{2m}, ranging from 0.83±0.01 in E3SM1 to 0.92±0.00 in CESM2. Regionally, GPCP estimates of variability lie within the ensembles' 2σ ranges over slightly more than half of the globe for all ensembles. In general, simulated P variability is too strong across much of the tropics and subtropics, as also found for T_{2m}, and too weak in the north tropical Atlantic Ocean and extratropics.

Increases in variability with time are simulated in all ensembles, with detectable increases from the piC to the past across broad portions of the tropics in E3SM2, CESM2, and CESM1HR. Into the present and future, these increases expand in area and intensity, being widespread across the Tropics in the present, and covering nearly the entire globe in the future. Isolated areas of decreased variability are also simulated in each ensemble, however these span a relatively small fraction of the globe. Future changes in precipitation variability positively correlate with the mean piC pattern, particularly in CESM1HR (PC=0.67), indicative of enhanced spatial gradients in variability. Increases in variability over land are particularly widespread, with over 86% of land regions experiencing detectable changes in the future, except CESM1SR which has a slightly lower fraction (79%), corresponding to increases in most regions. Past, present, and future changes in variability do not exhibit strong seasonality (Figs. S4, S5). Future patterns are generally consistent across ensembles, with the greatest increases in variability occurring in the deep tropics and isolated areas of decreased variability being confined to subsident subtropical regions. PCs with the MEM pattern are thus strong (≥0.84) for all ensembles except CESM1HR (PC=0.69), again highlighting the general consensus among SR models and the distinct form of projected changes in CESM1HR (Table S1). Ensemble-mean PCs of mean patterns against observations for CESM1HR (0.86±0.01) also lie on the lower end of the ensemble range (0.84-0.93) and the mean PC of CESM1HR is slightly weaker than that of CESM1SR. Changes generally emerge earlier in CESM1HR than the other ensembles with stronger patterns and more widespread changes over land simulated for the past and present than in CESM1SR or the other ensembles.

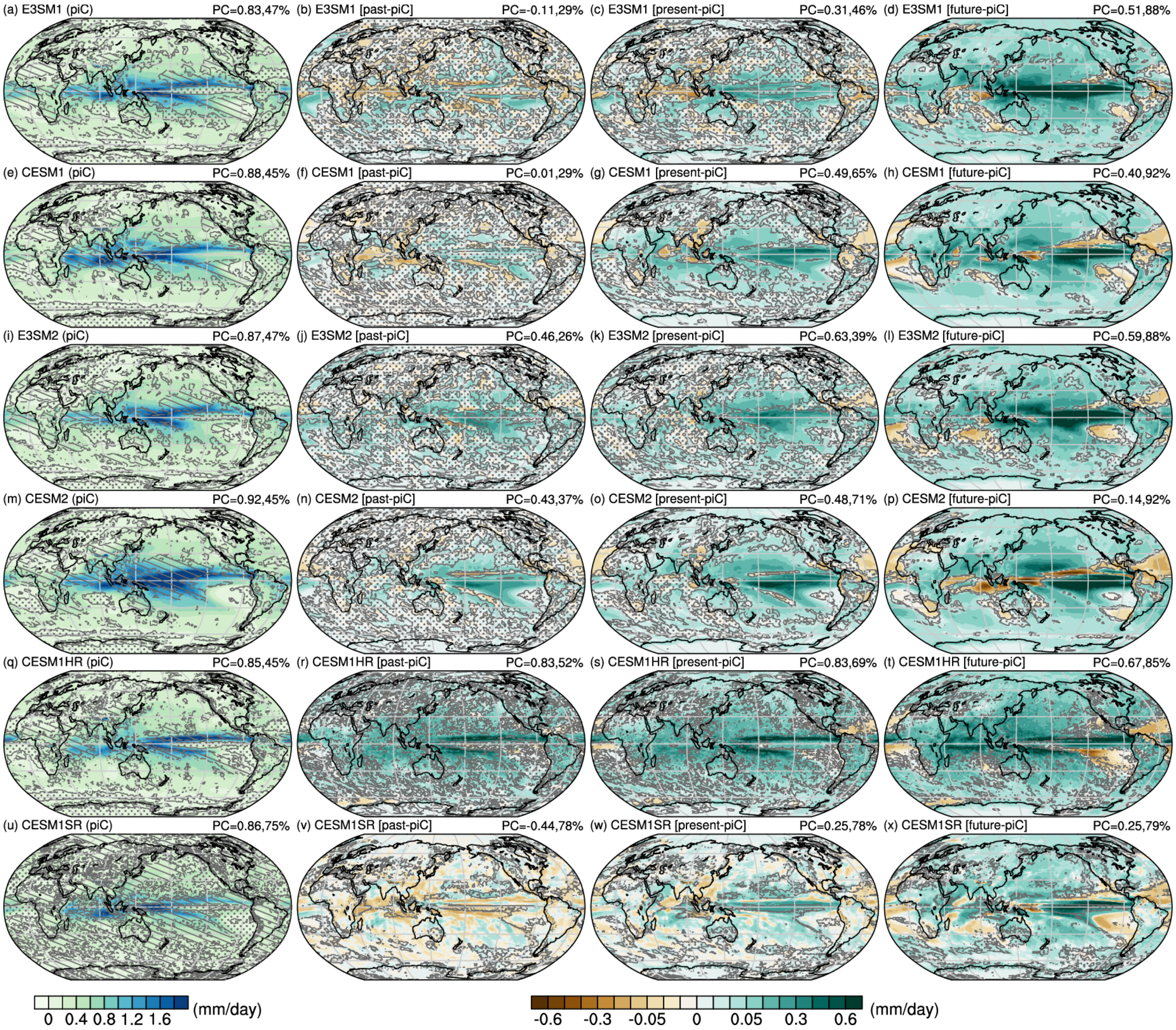

Figure 3: As in Figure 2 except for precipitation variability. The simulation interval used for observational evaluation in the left column is from 1979 to 2023 to match the period of GPCP, rather than 1950 to 2023 in Figure 2.

4. The El Niño / Southern Oscillation

Ensemble mean composite near-surface air temperature anomalies for December through February (DJF) during El Niño events generated by the CVDPv6 are shown in Figure 4 for the piC along with changes in the past, present, and future. The piC patterns (left column) are characterized generally by warm anomalies in the central and eastern equatorial Pacific Ocean, by construction, and remote warm anomalies in the equatorial Indian and Atlantic Oceans, the

Amazon and central Africa, and high-latitude regions east of the dateline. Cool anomalies are also simulated in a horseshoe pattern in the western and subtropical Pacific Ocean, though with some inconsistency across ensembles.

Despite a general tendency for models to simulate patterns that are too strong and shifted westward (Fasullo et al. 2020), simulated patterns agree generally with the observed pattern, with ensemble-mean pattern correlations ranging from a low of 0.50±0.06 (2-standard error range) in CESM1HR (Fig. 4q), to 0.69±0.01 in CESM2 (Fig. 4m), with about 22% to 37% of the globe exhibiting significant anomalies during El Niño events. The spread in PCs across ensembles is of the same order as the 2σ ranges (Table S2). The pattern in CESM1HR is systematically weaker than in CESM1SR, both in the equatorial Pacific and remote regions, and the percent of the globe with significant teleconnections is less (26% vs 37%). The ensemble-mean PC difference between CESM1HR and CESM1SR is much smaller than the 2σ range, though significant regional differences exist in the central equatorial and eastern subtropical Pacific Ocean.

There is a general tendency toward strengthening of El Niño composite patterns in all ensembles except CESM1HR that is detectable in many regions, even in the present, as found in other recent work (e.g. Wengel et al. 2021). Ensemble-mean global PCs of changes against the piC pattern are weak however for the future (-0.29 to 0.12), particularly in ensembles where T_{2m} variance decreases such as CESM2 (-0.28) and CESM1HR (-0.29), and thus the changes do not resemble the piC patterns. An increase in warm anomalies over many land regions is simulated across ensembles, though these increases are also less widespread in CESM1HR. In the instances of negative PCs, spatial gradients in the global pattern weaken, however a general tendency also exists toward increases in warm anomalies in tropical and subtropical land regions, where it strengthens the warming effects of El Niño. The PCs between each ensemble and the MEM for future changes are strong generally (≥0.71) except for CESM1HR (0.50), demonstrating a similarity across the SR ensembles that is not evident in CESM1HR (Table S1). Systematic differences between CESM1SR and CESM1HR El Niño composites are indicated by a lack of stippling in the bottom row of Fig. 4, with a weaker piC EM pattern and weaker changes generally by 2100 being simulated in CESM1HR.

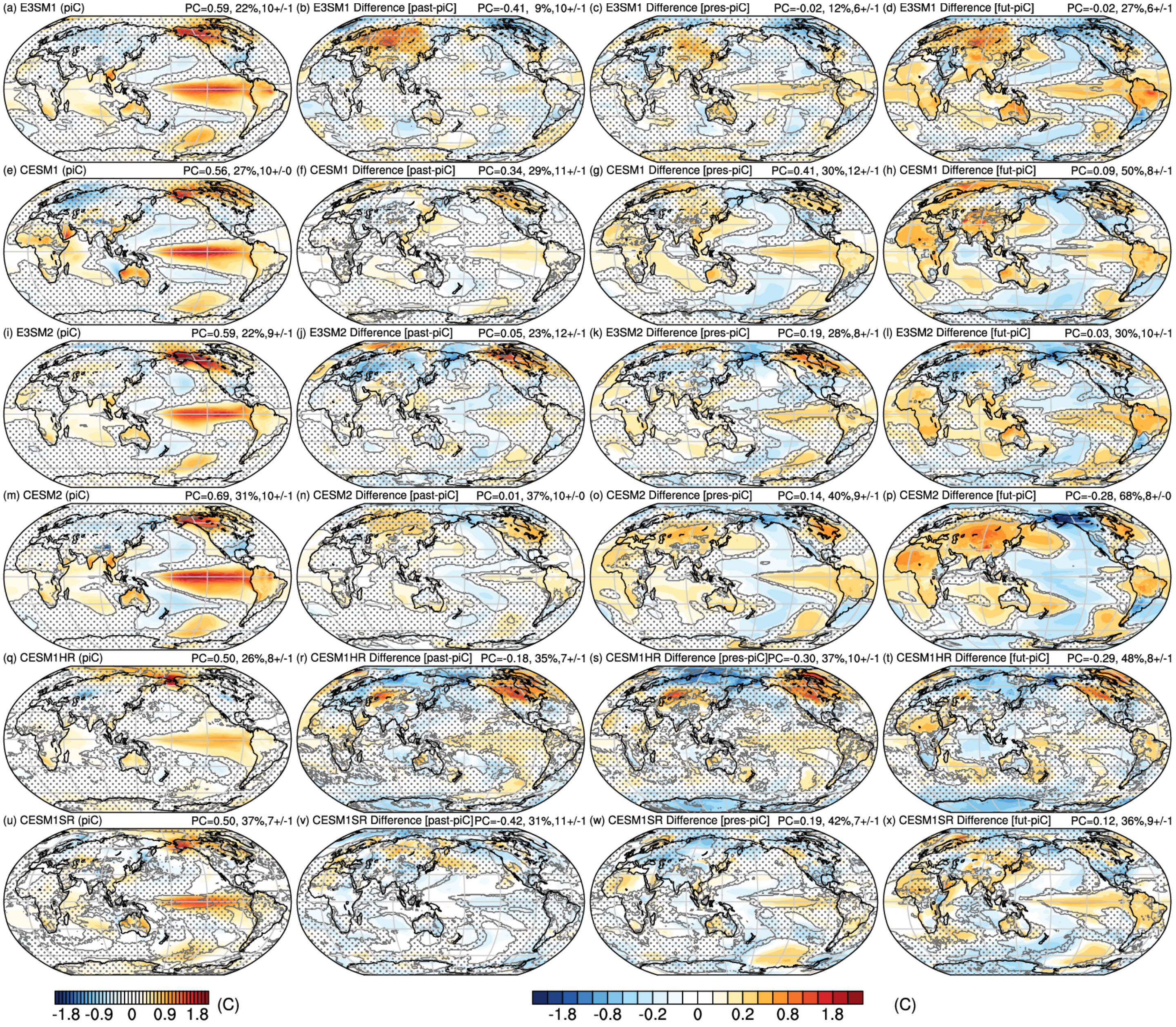
(a) E3SM1 (piC) PC=0.59, 22%,10+/-1
(b) E3SM1 Difference [past-piC] PC=-0.41, 9%,10+/-1
(c) E3SM1 Difference [pres-piC] PC=-0.02, 12%,6+/-1
(d) E3SM1 Difference [fut-piC] PC=-0.02, 27%,6+/-1
(e) CESM1 (piC) PC=0.56, 27%,10+/-0
(f) CESM1 Difference [past-piC] PC=0.34, 29%,11+/-1
(g) CESM1 Difference [pres-piC] PC=0.41, 30%,12+/-1
(h) CESM1 Difference [fut-piC] PC=0.09, 50%,8+/-1
(i) E3SM2 (piC) PC=0.59, 22%,9+/-1
(j) E3SM2 Difference [past-piC] PC=0.05, 23%,12+/-1
(k) E3SM2 Difference [pres-piC] PC=0.19, 28%,8+/-1
(l) E3SM2 Difference [fut-piC] PC=0.03, 30%,10+/-1
(m) CESM2 (piC) PC=0.69, 31%,10+/-1
(n) CESM2 Difference [past-piC] PC=0.01, 37%,10+/-0
(o) CESM2 Difference [pres-piC] PC=0.14, 40%,9+/-1
(p) CESM2 Difference [fut-piC] PC=-0.28, 68%,8+/-0
(q) CESM1HR (piC) PC=0.50, 26%,8+/-1
(r) CESM1HR Difference [past-piC] PC=-0.18, 35%,7+/-1
(s) CESM1HR Difference [pres-piC]PC=-0.30, 37%,10+/-1
(t) CESM1HR Difference [fut-piC] PC=-0.29, 48%,8+/-1
(u) CESM1SR (piC) PC=0.50, 37%,7+/-1
(v) CESM1SR Difference [past-piC]PC=-0.42, 31%,11+/-1
(w) CESM1SR Difference [pres-piC] PC=0.19, 42%,7+/-1
(x) CESM1SR Difference [fut-piC] PC=0.12, 36%,9+/-1
-1.8 -0.9 0 0.9 1.8
(C)
-1.8 -0.8 -0.2 0 0.2 0.8 1.8
(C)

Figure 4: Mean El Niño spatial composites of DJF air temperature anomalies (K) for the piC (left column), and the relative changes from the piC in past (center-left column), present (center-right column), and future (right column). Models shown include E3SM1 (a-d), CESM1, (e-h), E3SM2 (i-l), CESM2 (m-p), CESM1HR (q-t), and CESM1SR (u-x). Regions where piC composite magnitudes (left column) and changes (other columns) are not significantly different than zero are stippled (determined based on the 2 standard error range of each ensemble using 10 members), except for changes in the bottom row where they represent regions where differences from the CESM1HR are not significant. The values in the headers indicate the mean pattern correlations against observations from 1920 to 2023 and the percent of the globe regions that experience significant anomalies (left column) and pattern correlations with the mean piC pattern and percent of land regions exhibiting significant changes (other columns).

Ensemble-mean CVDPv6 composite precipitation anomalies during El Niño events are shown in Figure 5 for the piC along with changes in the past, present, and future. The patterns are characterized by positive anomalies in the central and eastern equatorial Pacific Ocean, the western equatorial Indian Ocean, and the eastern subtropical Pacific Ocean. Negative (e.g., dry) anomalies are generally simulated in the western Pacific Ocean and immediately poleward of the ITCZ, though with some inconsistency across ensembles. The mean PCs with observations are similar as for T_{2m}, with the weakest PC in CESM1HR (0.50±0.03) and the strongest in CESM2 (0.79±0.01). Significant anomalies span only a small percentage of the globe, ranging from 11% in E3SM2 to 25% in CESM1SR. The spread in PCs across ensembles is comparable in magnitude to the 2σ range (0.2, Table S2). Composite anomalies fail to be significant across most of the extratropics in all of the ensembles. The difference in the PC between CESM1SR and CESM1HR is not significant, although significant anomalies are more widespread in CESM1SR.

Changes over time in SR models are characterized by stronger positive anomalies in the central and eastern tropical Pacific Ocean and stronger negative anomalies in the Indo-Pacific warm pool and subtropical domains. Collectively these anomalies correlate positively with, and represent a strengthening of, the piC patterns in the present and future, except for the future in CESM2. They are also consistent with a strengthening of interannual variability across the ensembles, also shown in Fig. 3. PCs with the MEM pattern are generally strong (≥0.73) for all ensembles except CESM1HR (PC=0.35), again highlighting a general consensus among SR models and a distinct form of projected changes in CESM1HR. Key differences between CESM1SR and CESM1HR changes include weaker P anomalies across the deep Tropics being simulated in CESM1HR, consistent with the muted increases in warm anomalies (Fig. 4). For La

Niña , agreement in PCs of change with the MEM pattern is also strong (≥0.73), except for CESM1HR (PC=0.40, Table S1).

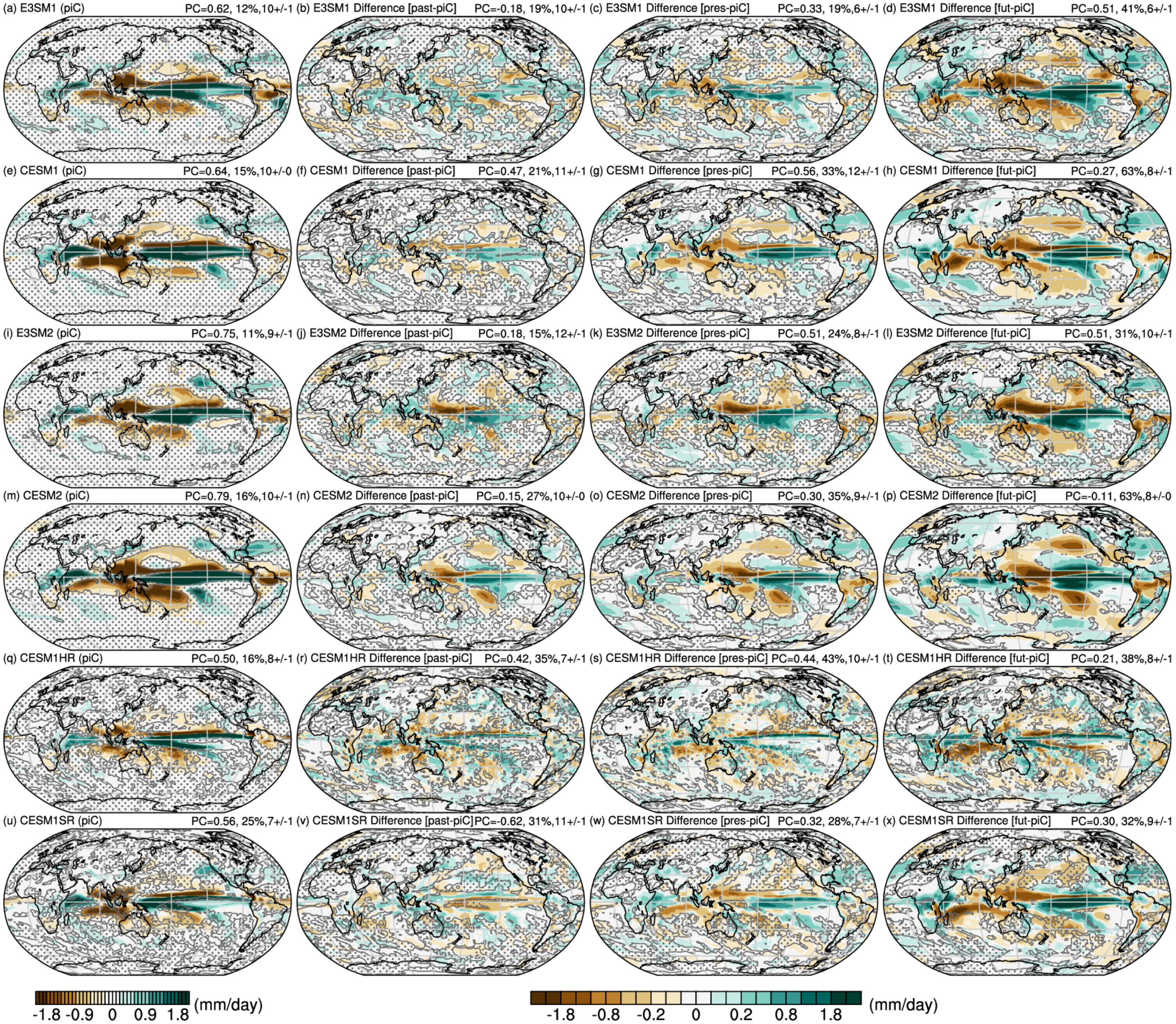

Figure 5: As in Fig. 4 but for fields of precipitation rather than T_{2m}.

Taylor diagrams summarizing pattern correlations and strengths across ensembles are shown in Figure 6. The plots use observations as a reference point and provide a means for evaluating ensemble spread and comparing present and future patterns via ensemble mean values. Considerable intra-ensemble spread exists due to the influence of internal variability.

Generally this spread is larger for the σ of patterns (distance from origin) than for the PCs (radial angle), illustrating the relative utility of PCs as a benchmark for model evaluation and inter-comparison where ensembles are not available. Changes in T_{2m} patterns during both El Niño (Fig. 7a) and La Niña (Fig. 7b) are modest generally and characterized by incremental changes, except for E3SM1, in which a modest increase in σ is evident, and CESM1HR, in which a modest reduction exists. Changes in P are consistently characterized by increases in σ, except in CESM1HR, where marginal reductions are evident. All ensemble-mean changes fall within the intra-ensemble present-day ranges, highlighting the importance of intrinsic variability in the outcome of any single realization.

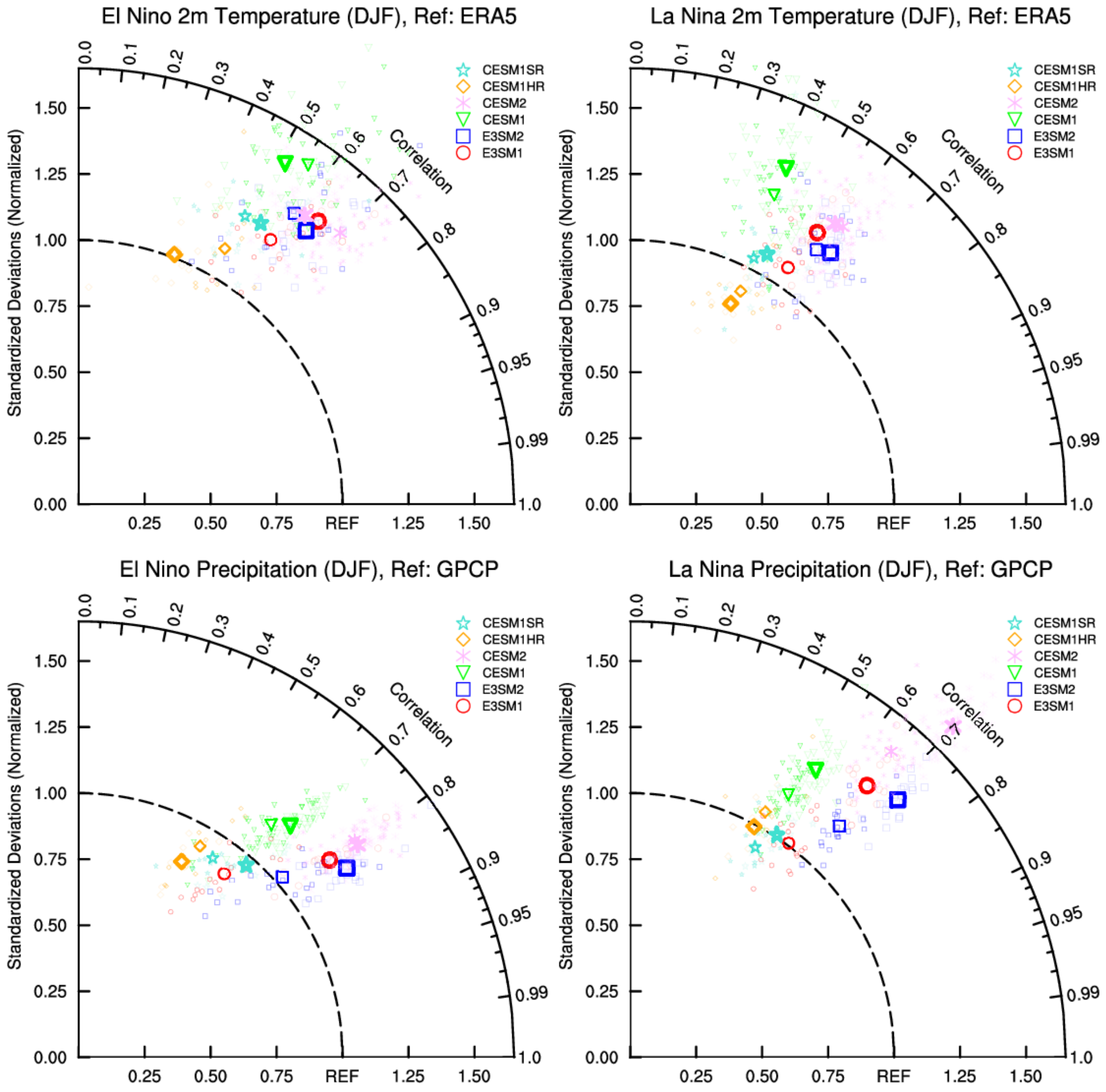

Figure 6: Taylor diagram of global El Niño (left) and La Niña (right) DJF composites of temperature (top) and precipitation (bottom) anomalies for multiple model ensembles using ERA5 (top) and GPCP (bottom) for reference datasets. Small bold symbols depict ensemble-mean values for the observational era whereas large bold symbols represent future ensemble-mean values.

To address important spatio-temporal aspects of ENSO in the equatorial Pacific Ocean, ensemble-mean hovmoëllers (HOV) of temperature anomalies during El Niño events generated by the CVDPv6 are shown in Figure 7 for the piC and past, present, and future changes. A companion analysis for La Niña composites is presented in Figure S6. The piC patterns (left column) are characterized by both warm anomalies in the central and eastern equatorial Pacific Ocean during boreal winter, largely by construction, that transition to cool anomalies a year later in some of the ensembles in a manner consistent with observations (not shown). A failure to simulate sufficient delayed cooling a year after peak warming is evident in E3SM1, CESM1 and CESM1HR/SR, while E3SM2 and CESM2 lie closer to observations. Associated with this lack of delayed cooling, La Niña events in CESM1HR/SR are also generally much too weak.

Inter-ensemble contrasts are notable, both in regards to the strength and zonal breadth of anomalies at the peak of El Niño (Jan 1), and the transition to cool anomalies a year later. Simulated patterns agree generally with those observed, with ensemble-mean pattern correlations ranging from a low of 0.79±0.03 in CESM1HR (Fig. 7q) to a high of 0.91±0.00 in CESM2 (Fig. 7m) with about 37% to 61% of the domain exhibiting significant anomalies. The spread in PCs across ensembles is only slightly larger than the 2σ range of order 0.04 (Table S2). Systematic differences between CESM1SR and CESM1HR are also notable with a detectable weakening at the onset of events and diminished cooling afterwards in CESM1HR. The mean PC for CESM1HR (0.79±0.03) is smaller than that for CESM1SR (0.85±0.01), a difference on the order of the 2σ range.

Changes in time are similar generally across the ensembles, with increases at the peak of events across the basin and decreases in the year following events, changes that are evident in the present and particularly strong in the future. Changes in La Niña however are strongly model dependent (Fig. S6, right column). Future changes correlate positively with piC patterns for both El Niño and La Niña and thus represent a strengthening of variability, consistent with Figs. 2 and 4, though with some model dependence in pattern details. For El Niño, PCs with the MEM future pattern are generally strong (≥0.76) except CESM1HR (PC=0.69), again highlighting a general consensus among SR models that is less evident in CESM1HR (Table S1). For La Niña, the future change in the pattern also correlates well with the MEM (≥0.73) with somewhat weaker agreement for CESM1HR (PC=0.64).

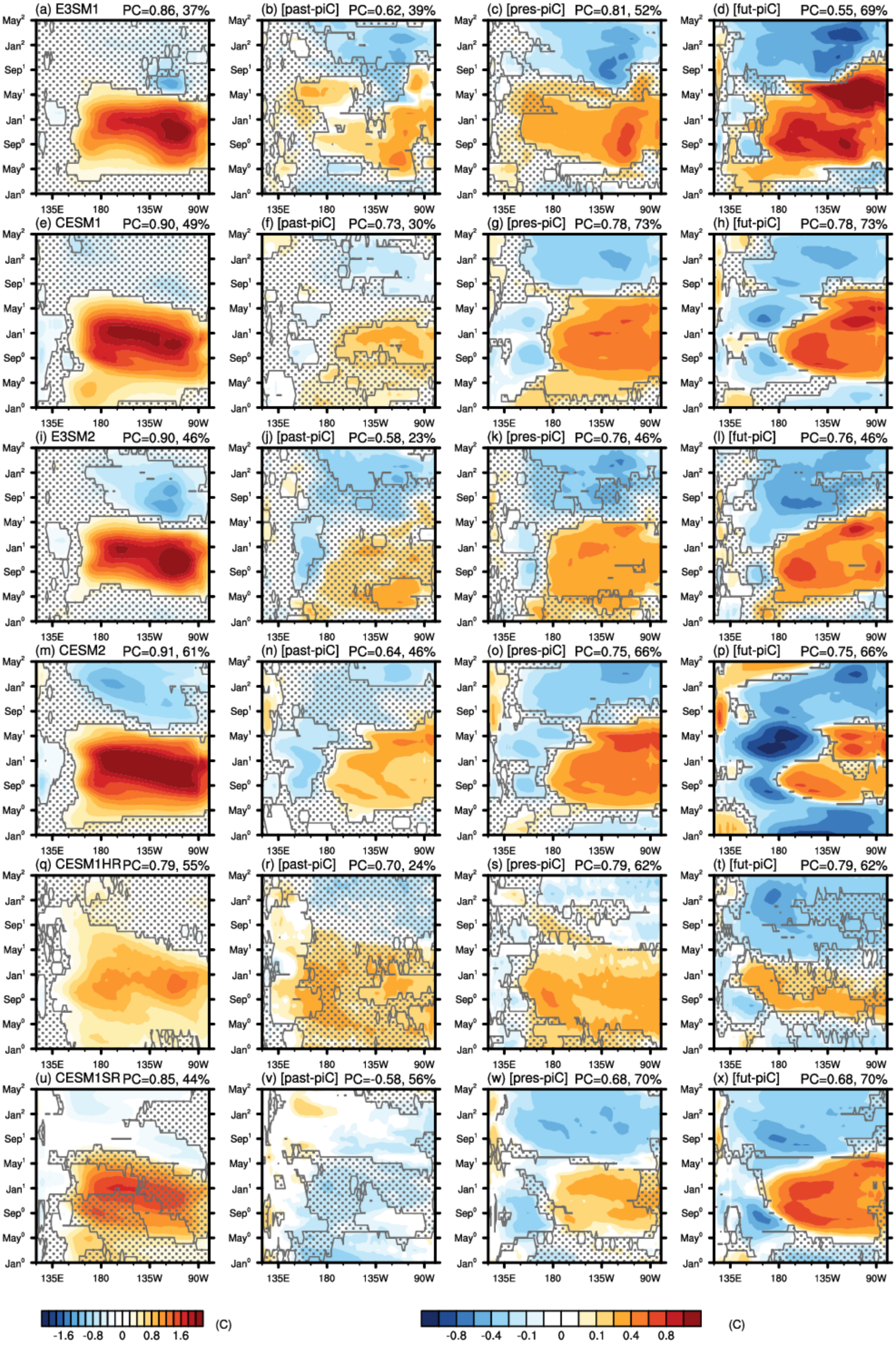
(a) E3SM1 PC=0.86, 37%
(b) [past-piC] PC=0.62, 39%
(c) [pres-piC] PC=0.81, 52%
(d) [fut-piC] PC=0.55, 69%
(e) CESM1 PC=0.90, 49%
(f) [past-piC] PC=0.73, 30%
(g) [pres-piC] PC=0.78, 73%
(h) [fut-piC] PC=0.78, 73%
(i) E3SM2 PC=0.90, 46%
(j) [past-piC] PC=0.58, 23%
(k) [pres-piC] PC=0.76, 46%
(l) [fut-piC] PC=0.76, 46%
(m) CESM2 PC=0.91, 61%
(n) [past-piC] PC=0.64, 46%
(o) [pres-piC] PC=0.75, 66%
(p) [fut-piC] PC=0.75, 66%
(q) CESM1HR PC=0.79, 55%
(r) [past-piC] PC=0.70, 24%
(s) [pres-piC] PC=0.79, 62%
(t) [fut-piC] PC=0.79, 62%
(u) CESM1SR PC=0.85, 44%
(v) [past-piC] PC=-0.58, 56%
(w) [pres-piC] PC=0.68, 70%
(x) [fut-piC] PC=0.68, 70%
May^2
Jan^2
Sep^1
May^1
Jan^1
Sep^0
May^0
Jan^0
135E
180
135W
90W
-1.6
-0.8
0
0.8
1.6
(C)
-0.8
-0.4
-0.1
0
0.1
0.4
0.8
(C)

Figure 7: Mean El Niño hovmoëllers of sea surface temperature (SST) composite for the piC (left column), and the relative changes from the piC in past (center-left column), present (center-right column), and future (right column). Models shown include E3SM1 (a-d), CESM1, (e-h), E3SM2 (i-l), CESM2 (m-p), CESM1HR (q-t), and CESM1SR (u-x). Regions of insignificant anomalies (left column) and differences (other columns) are stippled, except in the bottom row where they denote insignificant differences with CESM1HR.

5. Modes Strongly Coupled to ENSO

The Indian Ocean Dipole

Ensemble-mean IOD patterns, generated in the CVDPv6 from regression of the IOD index against T_{2m}, are shown in Figure 8 for the piC and changes in the past, present, and future. The patterns are characterized by warm anomalies in the western Indian Ocean and cool anomalies in the east, offset to the north and south from the equator in the west and east, respectively. Statistically significant anomalies tied to the IOD are found across much of the Indian Ocean, though teleconnections in the Southern Indian Ocean are weak in the E3SM ensembles. PCs against observations are strong generally ($\geq$0.69) with detectable anomalies over more than 58% of the domain in all ensembles. The spread in PCs across ensembles is only slightly larger than the 2σ range of order 0.04 (Table S1). The general form of the IOD and the strength of PC against observations agree closely between CESM1SR and CESM1HR.

Changes in the IOD over time are strongly model dependent with some ensembles showing persistent positive correlations with the piC pattern (E3SM2, CESM1SR/HR), while other ensembles exhibit PCs that vary in sign with time. In some ensembles, such as CESM1, projected changes represent a strengthening of the piC pattern whereas in others, such as CESM2, they represent a weakening. PCs with the MEM pattern span a wide range, varying from 0.17 in CESM2 to 0.94 in CESM1HR, indicating significant structural uncertainty in projected changes in the IOD. The effect of resolution is marginal however, with strong similarity between present and future patterns in CESM1HR and CESM1SR (Figs. 8s, t, w, x).

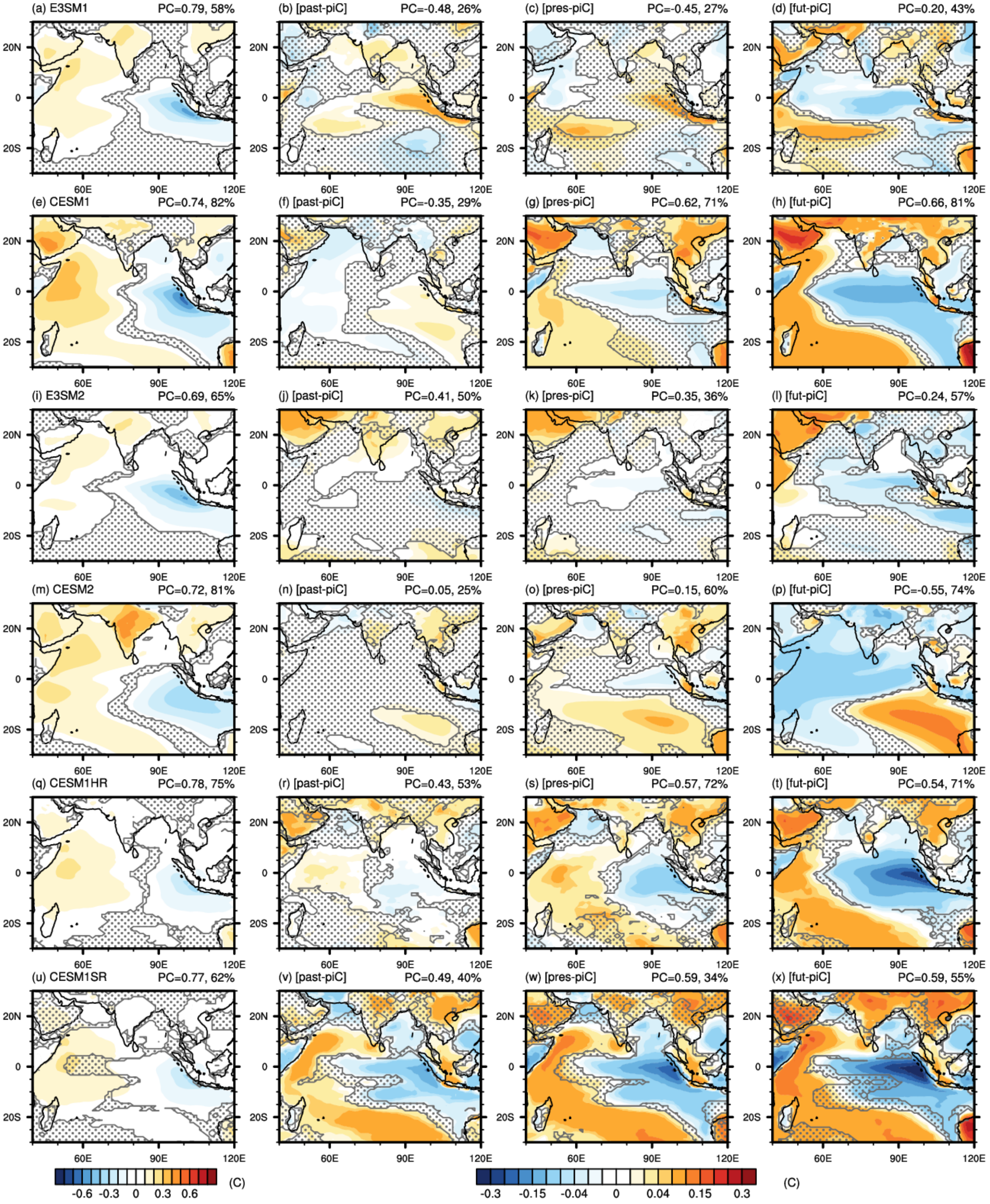

Figure 8: Indian Ocean Dipole patterns generated from regression onto T_{2m}, consistent with the conventions used in Figure 4.

Pacific Decadal Variability

Ensemble-mean regressed T_{2m} anomalies associated with PDV generated by the CVDPv6 are shown in Figure 9 for the piC along with changes in the past, present, and future. The patterns are characterized by both a zonal dipole of anomalies in the North Pacific Ocean and warm anomalies in the eastern tropical Pacific Ocean in most ensembles. The greatest inter-ensemble contrast is associated with the strength and breadth of warm anomalies in the equatorial Pacific, features that have been highlighted in previous work differentiating climate models generally (Fasullo et al. 2020).

Despite a general tendency for models to simulate patterns that are too weak in the tropical Pacific Ocean (Fasullo et al. 2020), simulated patterns agree generally with those observed, with ensemble-mean global PCs ranging from a low of 0.70±0.07 in E3SM1 (Fig. 9a) to a high of 0.80±0.02 in CESM1SR (Fig. 9u) with a wide range in the percent of the globe exhibiting significant teleconnections (11% in E3SM2 to 41% in CESM2). The spread in PCs across ensembles is smaller than the 2σ range, which is approximately 0.1 but is also strongly model dependent. Regions of strong PDV association also vary considerably across models, with some models exhibiting significant teleconnections confined mainly in the North Pacific (e.g. E3SM2), while others, particularly in cases of strong equatorial signals, exhibit significant teleconnections across the tropics and SH (e.g. CESM2). Model resolution also exerts an influence on these features, with CESM1HR exhibiting stronger teleconnections in the tropics and coastal Antarctic regions than CESM1SR.

Changes in time represent an El Niño-like shift in the tropics in the ensembles where El Niño composites also strengthen (E3SM1, CESM1, E3SM2, CESM1SR, Fig. 4) and systematically different patterns of change in the Tropics in CESM2 and CESM1HR. Whether projected changes represent a strengthening of the piC pattern is also model dependent, with positive PCs in some ensembles (e.g. CESM1) and negative PCs in others (e.g. CESM2). Given these contrasts, PCs with the MEM pattern are mixed, ranging from 0.03 in CESM2 to 0.88 in E3SM2, confirming a large structural uncertainty in projected changes. Changes over time also exhibit a dependence on resolution, with changes occurring earlier in CESM1HR than CESM1SR and future changes in the Tropics being strongly different.

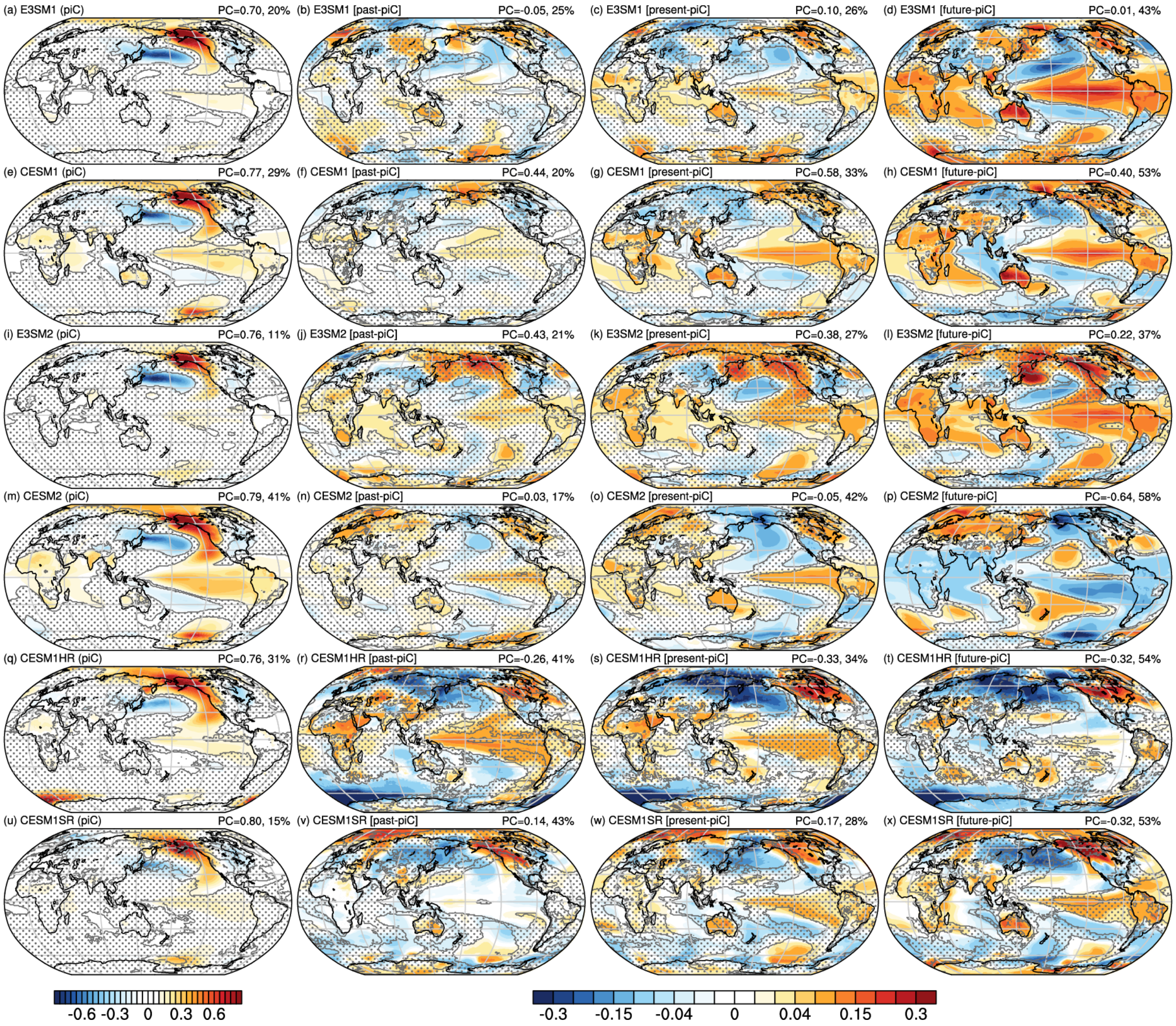

Figure 9: As in Fig. 8 but for Pacific Decadal Variability.

The North Pacific Meridional Mode

Ensemble-mean NPMM patterns, generated in the CVDPv6 from regression of the NPMM index against SST, are shown in Figure 10 for the piC and for changes in the past, present, and future. The patterns are characterized by a dipole in the central and eastern north subtropical Pacific Ocean, with statistically significant teleconnections extending into the Tropics and northern high latitudes. Contrasts in both the magnitude and spatial extent of teleconnections are evident across ensembles. Simulated patterns agree generally with those observed, with mean ensemble pattern correlations ranging from a low of 0.56±0.17 in E3SM1 (Fig. 10a) to 0.84±0.01 in E3SM2 (Figs. 10i) with a broad range in the percent of the Northern

Hemisphere (NH) ocean exhibiting significant teleconnections (10% in CESM2 to 25% in CESM1SR). The significance of the spread in PCs across ensembles is difficult to determine due to the broad spread in 2σ ranges across ensembles (Table S2). The NPMM pattern is systematically stronger in CESM1HR versus CESM1SR, particularly for mode's warm regions, and the PC with observations degrades (Figs. 10q, u).

Projected changes in the NPMM are strongly model dependent and are characterized by warming in the central Pacific Ocean and cooling in the other ocean basins in the NH, a pattern that is particularly strong in CESM2. In E3SM1, future changes correlate positively with the piC pattern, though such correspondence is weak in the other ensembles. PCs with the MEM pattern are modest to strong ranging from 0.43 in E3SM1 to 0.93 in CESM1, with the exception of a small PC in CESM1HR (PC=0.17), again illustrating a general consensus among SR models and distinct form of changes in CESM1HR. In comparing CESM1HR and CESM1SR (Fig. 10q-t vs Fig 10u-x), changes in most NH regions are impacted by model resolution (lack of stippling).

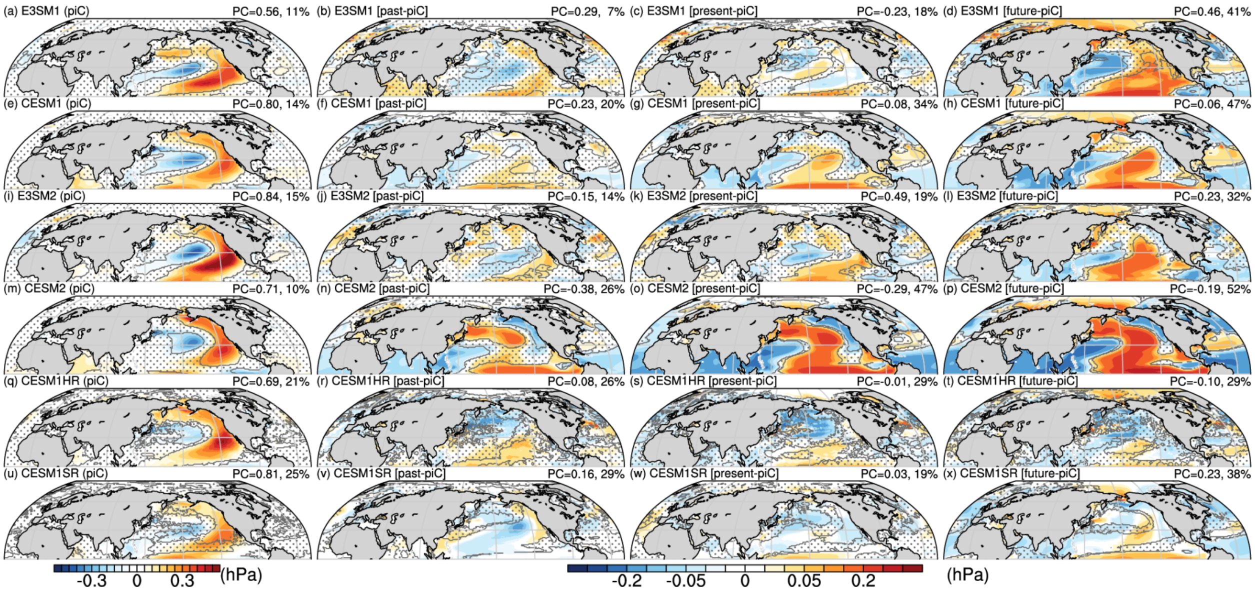

Figure 10: As in Fig. 8 but for the North Pacific Meridional Mode.

6. Extratropical Modes

Ensemble-mean regressed SST anomalies associated with AMV generated by the CVDPv6 are shown in Figure 11 for the piC along with changes in the past, present, and future. The patterns are characterized by horseshoe-shaped warm anomalies extending across the North Atlantic Ocean, to northern Africa and the northern subtropical Atlantic Ocean, as also shown by Deser and Phillips (2023). In some models, teleconnections (e.g. CESM1HR) also extend into the tropical and eastern Pacific Ocean from 60ºN to 60ºS. Global PCs against observations are generally modest, ranging from 0.48±0.04 in CESM1HR to 0.71±0.03 in CESM1. Less than 26% of the global ocean exhibits detectable teleconnections, with an extent that is particularly small in E3SM1 (7%) and E3SM2 (9%). The significance of inter-ensemble biases is limited by their large 2σ range, which is of order 0.2 (Table S2). The effects of resolution on the pattern are modest, with CESM1HR and CESM1SR exhibiting broad agreement, with the main effect being a strengthening of the pattern in CESM1HR in some regions (e.g. North Atlantic and Indian Oceans).

Changes in time vary widely across ensembles, with many of the strongest changes occurring outside of the North Atlantic Ocean, except for E3SM2. The strongest and more persistent simulated changes occur in CESM2, characterized by warm anomalies in much of the tropical oceans in all periods, features that are also generally evident in CESM1 in the present and future and E3SM1 in the future. Other ensembles show different patterns, with CESM1SR and CESM1HR showing more extensive cold than warm anomalies in the Tropics and broad agreement in their patterns overall. Despite the contrasts across ensembles in the Tropics, global-ocean PCs with the MEM pattern are generally modest to strong (≥0.68) for all ensembles except CESM1HR (PC=0.54), again highlighting the distinct form of its projected changes.

Atlantic Multidecadal Variability

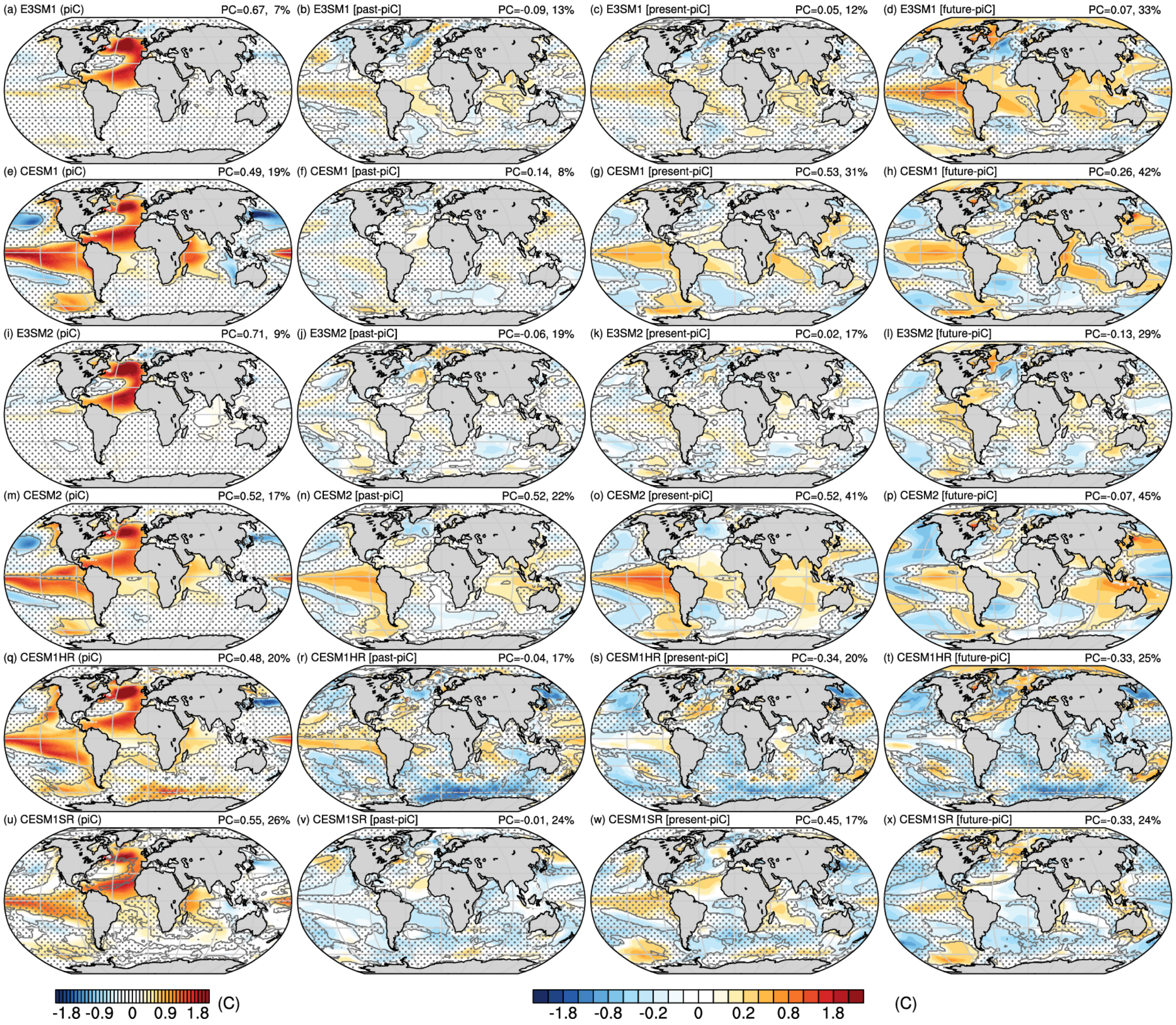

Figure 11: As in Fig. 8 but for Atlantic Multi-Decadal Variability.

The Southern Annular Mode

Ensemble-mean regressed SLP anomalies associated with the JJA SAM, generated by the CVDPv6, are shown in Figure 12 across ensembles for the piC along with changes in the past, present, and future. The patterns are characterized by anomalous high pressure across much of the Southern Ocean and low pressure in Antarctica and its neighboring coastal zones. Despite a general tendency for models to simulate patterns that are displaced southward from the observed pattern (Fasullo et al. 2020), the regional PCs with observations are high generally, ranging from a low of 0.93±0.01 in CESM2 (Fig. 12m) to 0.98±0.01 in CESM1 and CESM1HR (Figs. 12e, q).

The spread in PCs across ensembles is smaller than the 2σ range of order 0.06, however, limiting statements on model fidelity. The main inter-model contrasts are associated with the pattern strength over Antarctica and structure just south of Australia. More than 45% of the SH exhibits detectable teleconnections with the SAM in each ensemble, with a maximum extent of 75% in CESM1HR.

Simulated changes in the SAM in SR ensembles are characterized generally by increased pressure over Antarctica and intensification of a wavenumber 3 structure evident near 40ºS, that is similar in structure but longitudinally shifted from the piC pattern in some models. The offset results in future changes that are strongly negatively correlated with the piC pattern in some ensembles, such as CESM1 (PC=-0.54) and CESM2 (PC=-0.80). PCs with the MEM pattern are generally modest to strong (between 0.43 to 0.86) for all ensembles except CESM1HR (PC=0.30), which again exhibits the weakest PC with the MEM. Differences in projected patterns between CESM1SR and CESM1HR are small generally, though the extent of significant changes over land increases from 54% to 25% with increased resolution.

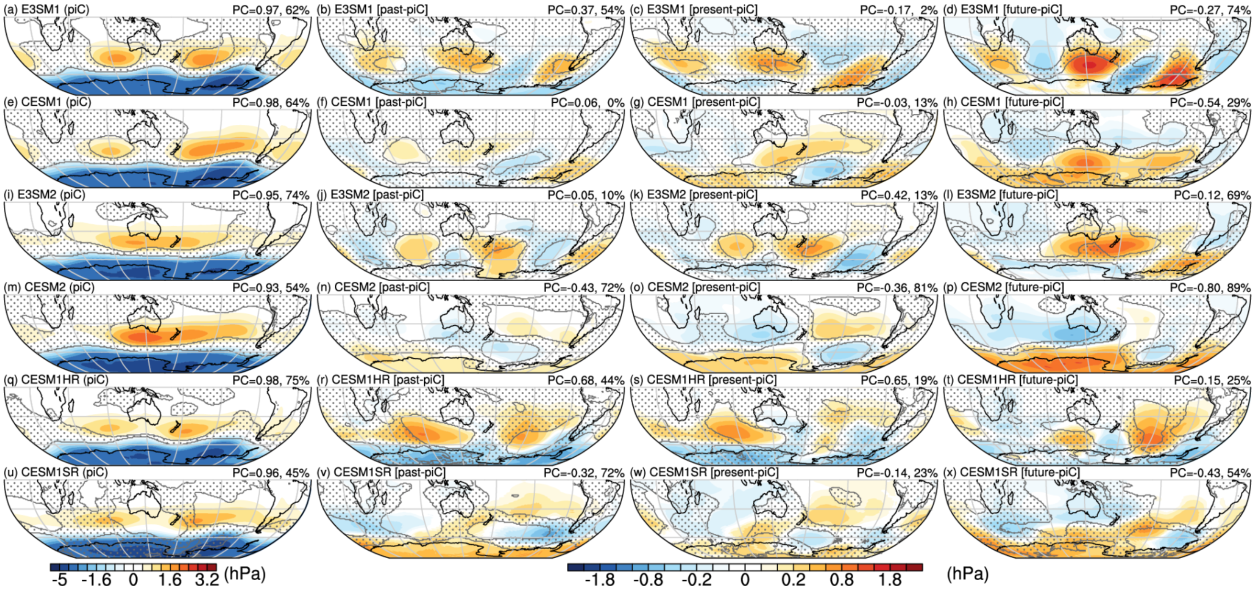

Figure 12: As in Fig. 8 but for JJA SAM SLP.

The Pacific / North America Mode

Ensemble-mean PNA patterns, generated in the CVDPv6 from regression of the PNA index against SLP in DJF, are shown in Figure 13 for the piC and for changes in the past, present, and future. The patterns are characterized by strong negative anomalies in the Aleutian Low and positive values across much of the Arctic. Mean PCs with observations range from 0.86±0.02 in CESM1SR to 0.93±0.01 in CESM2, though the spread in PCs across ensembles is of the same order as the 2σ range (0.05, Table S2). Statistically detectable PNA teleconnections are found across a large percentage of the NH, ranging from 40% in E3SM2 and CESM1SR to 69% in CESM1HR.

Simulated changes from the piC pattern are characterized generally by intensification of the Aleutian Low and increased pressure in northern Eurasia. These features contribute to positive PCs between future changes and piC patterns, ranging from 0.35 in CESM2 to 0.84 in CESM1HR, leading to an intensification of PNA SLP anomaly gradients in all ensembles. Emergence of the changes is soonest in CESM1HR, which exhibits a detectable deepening of the Aleutian Low in the past, present, and future, with significantly stronger patterns and earlier emergence of changes in CESM1HR versus CESM1SR. PCs of future patterns with the MEM are generally modest to strong across ensembles, ranging from 0.45 in CESM2 to 0.92 in CESM1. In contrast to other modes, the PC of CESM1HR with the MEM lies in the middle of the SR distribution.

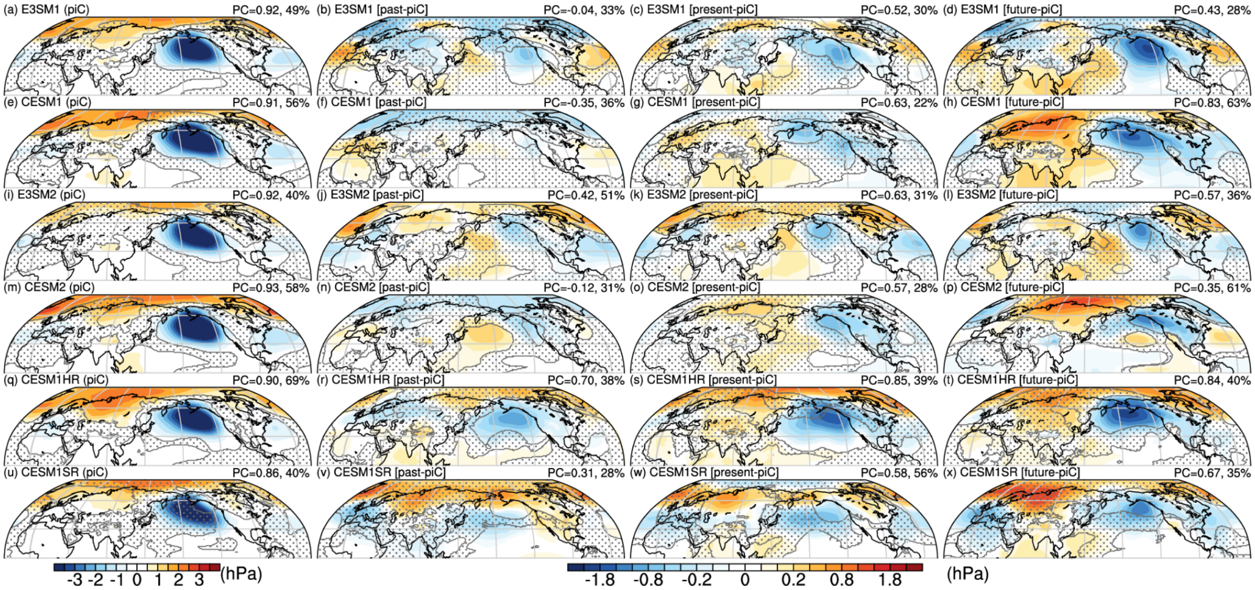
(a) E3SM1 (piC) PC=0.92, 49%
(b) E3SM1 [past-piC] PC=-0.04, 33%
(c) E3SM1 [present-piC] PC=0.52, 30%
(d) E3SM1 [future-piC] PC=0.43, 28%
(e) CESM1 (piC) PC=0.91, 56%
(f) CESM1 [past-piC] PC=-0.35, 36%
(g) CESM1 [present-piC] PC=0.63, 22%
(h) CESM1 [future-piC] PC=0.83, 63%
(i) E3SM2 (piC) PC=0.92, 40%
(j) E3SM2 [past-piC] PC=0.42, 51%
(k) E3SM2 [present-piC] PC=0.63, 31%
(l) E3SM2 [future-piC] PC=0.57, 36%
(m) CESM2 (piC) PC=0.93, 58%
(n) CESM2 [past-piC] PC=-0.12, 31%
(o) CESM2 [present-piC] PC=0.57, 28%
(p) CESM2 [future-piC] PC=0.35, 61%
(q) CESM1HR (piC) PC=0.90, 69%
(r) CESM1HR [past-piC] PC=0.70, 38%
(s) CESM1HR [present-piC] PC=0.85, 39%
(t) CESM1HR [future-piC] PC=0.84, 40%
(u) CESM1SR (piC) PC=0.86, 40%
(v) CESM1SR [past-piC] PC=0.31, 28%
(w) CESM1SR [present-piC] PC=0.58, 56%
(x) CESM1SR [future-piC] PC=0.67, 35%

Figure 13: As in Fig. 8 but for DJF PNA SLP.

The North Atlantic Oscillation

Ensemble-mean regressed SLP anomalies associated with NAO generated by the CVDPv6 are shown in Figure 14 for the piC, along with changes in the past, present, and future. The patterns are characterized by a meridional dipole of anomalies in the northeast Atlantic Ocean, with detectable negative anomalies spanning much of the Arctic and detectable positive anomalies covering much of the northern Pacific and Atlantic Oceans. Despite a general tendency for models to simulate patterns that are too weak (Fasullo et al. 2020), agreement with the observed pattern is strong, with mean PCs ranging from 0.89±0.04 in CESM1HR to 0.93±0.01 in CESM1SR. Differences in PCs across ensembles are similar in magnitude to the 2σ range of ~0.05 (Table S2) and thus relative model fidelity is unclear. Based on differences between CESM1SR and CESM1HR, the impact of increasing resolution is to weaken anomalies generally over much of the Arctic and increase them in the North Pacific Ocean (Figs. 14q, u).

Simulated changes are characterized generally by increases in the Aleutian Low and decreases across much of the Arctic, though with considerable model dependence. PCs between future changes and the piC pattern vary widely, from -0.33 in CESM2 to 0.60 in CESM1HR, with the spatial extent of significant changes being widespread. There is therefore considerable structural uncertainty in projections of NAO pattern strength. PCs of changes with the MEM pattern are modest to strong, ranging from 0.52 in CESM1HR to 0.89 in CESM2. Other SR models correlate weakly with the MEM (0.55 in E3SM1) and thus CESM1HR is not an outlier. The influence of resolution on NAO projections is also unclear as projected future changes are highly similar in form between CESM1HR and CESM1SR.

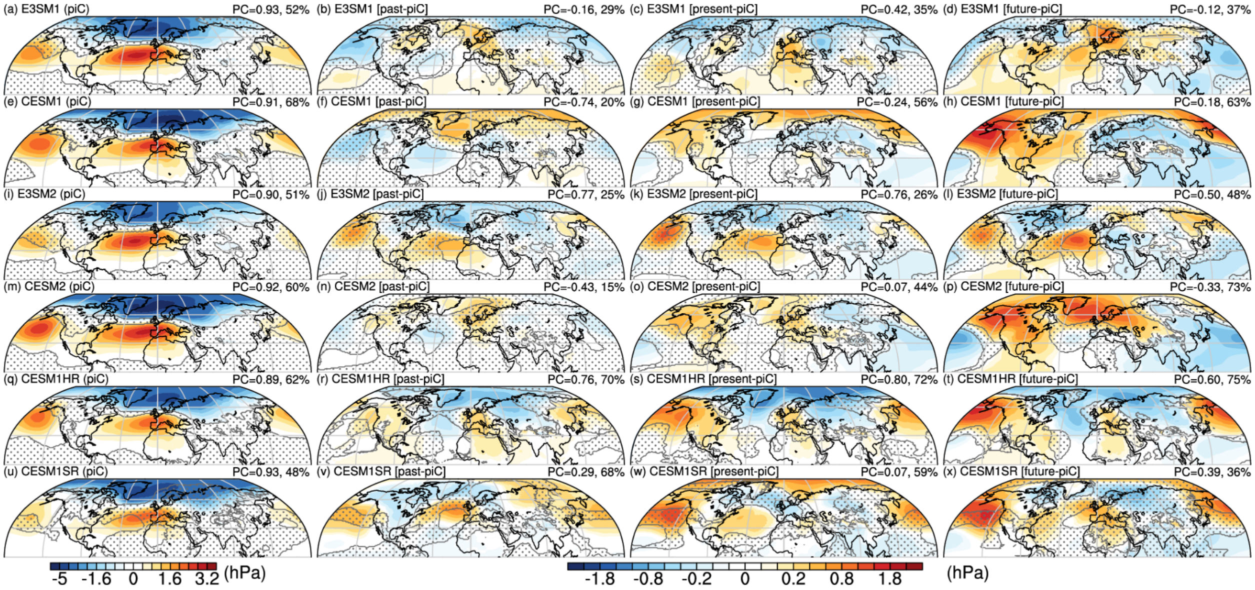

Figure 14: As in Fig. 8 but for DJF NAO SLP.

7. Additional Analyses

In Figure 15 the robustness of forced MoV changes identified in earlier work is examined in the ensembles used herein. These include a decoupling of the NAO from the Arctic Oscillation (AO, Hamouda et al. 2021), an increase in SST variance in the Niño3.4 region (Wang et al. 2019), a reduction in NAO variance in DJF (Fuentes-Franco et al. 2023), and a change in the seasonality of the IOD (Zheng et al. 2021, Sun et al. 2022). For the NAO-AO coupling, ensemble median changes in the NAO-AO PC are generally very small. Some members of E3SM1, E3SM2 and CESM2 exhibit strong decreases (>0.3) while in CESM1 and CESM1HR individual members can also exhibit strong increases (>0.3) but these changes are indicative mainly of intrinsic variability in the PC, which is also model dependent. Changes in SST variance in the Niño3.4 region are positive generally, though in two ensembles (CESM2 and CESM1HR), they are not distinguishable from zero. Changes in CESM1HR are particularly small and have been argued to reflect a more realistic representation of latent heat flux damping and advective feedbacks (Wengel et al. 2021).

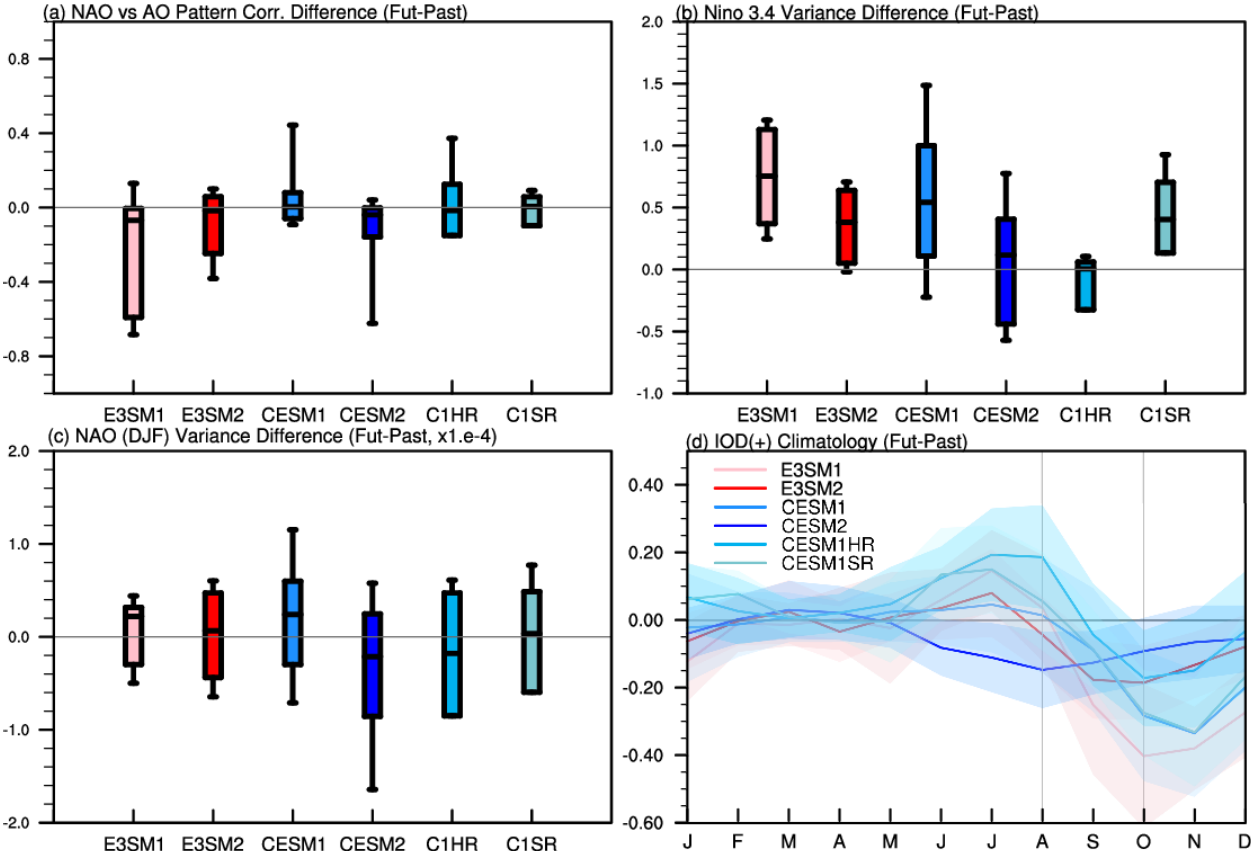

Figure 15: Robustness of Mode Changes: Future changes from piC in (a) the pattern correlation between DJF NAO and AO, (b) Niño3.4 SST variance, (c) NAO variance in DJF, and (d) the composite positive phase of the IOD by month of year.

Lastly, in Figure 16, the root-mean-squared-error (RMSE) of mode indices are compared when approximations of forced signals are employed using the various approaches in the CVDPv6 (see Methods) as compared to mode indices computed via explicit removal of the ensemble mean. For SLP (ie, circulation) -based modes, removal of a linear fit outperforms other CVDPv6 methods, which include removal of a quadratic fit or 30-year running mean. This suggests that linear fits of SLP based modes, particularly in the modes' extratropical domains where internal variability is large, are less susceptible to the introduction of noise than other methods. For temperature (ie, SST) -based modes, error ranges are particularly large for modes with indices that alias aerosol forcing, including PDV and NPMM, and the best-performing approach is mode and model dependent. For some modes, such as PDV and NPMM, linear detrending performs particularly poorly due to apparent cooling in the indices in the mid 20th century. For the AMV, 30-year running mean removal performs best. Optimal methods are generally mixed for other modes, though linear detrending is rarely an optimal method for temperature-based modes.

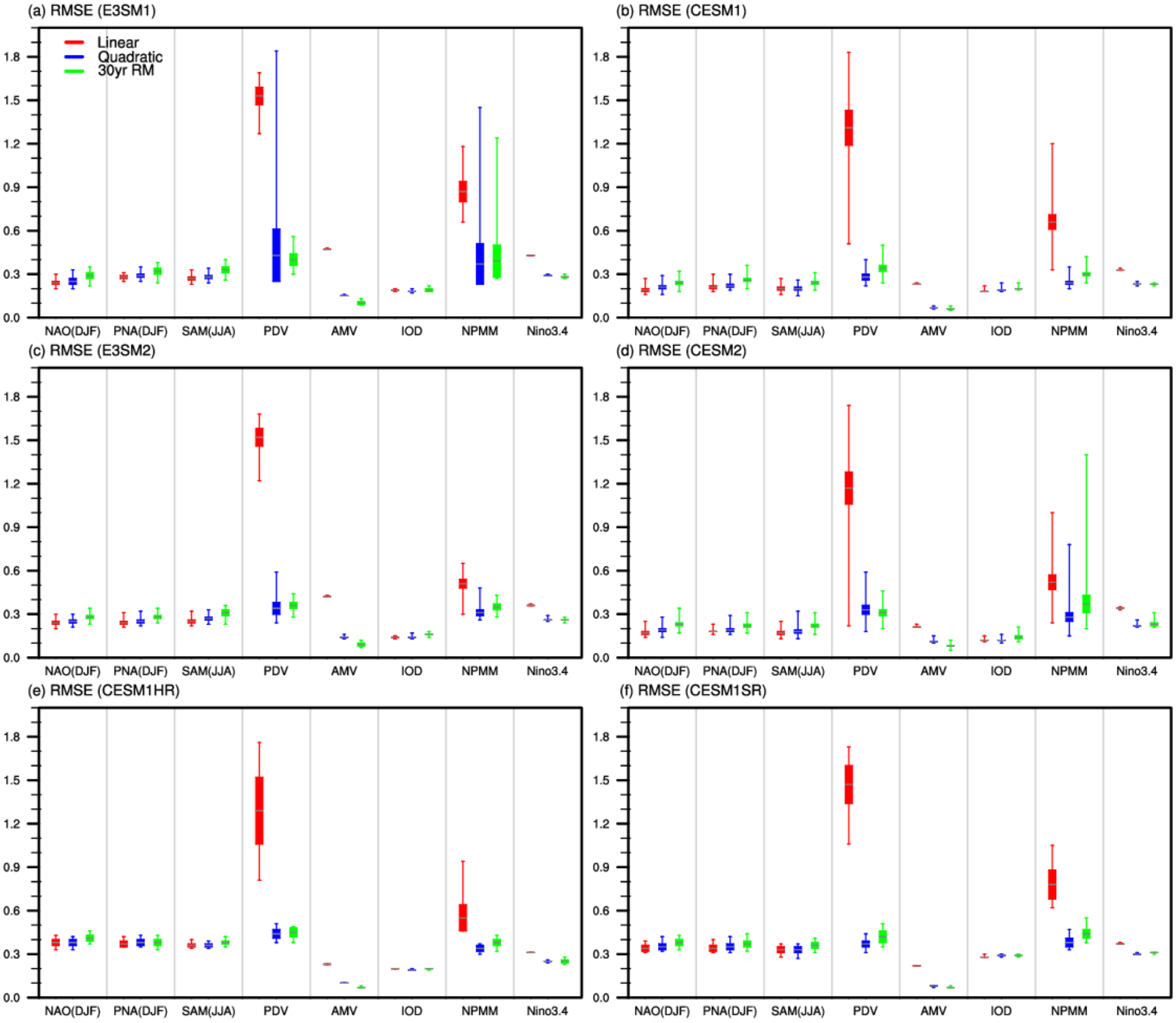

Figure 16: Root mean-squared error (RMSE) for various approaches of removing the forced response from mode indices relative to removal of the ensemble mean. Values plotted are provided in Table S3.

7. Summary and Conclusions

Using the newly developed CVDPv6 and multiple climate model ensembles, including four large ensembles and two 10-member ensembles, one of which is high-resolution, we have examined model fidelity in simulating a broad range of MoV, the susceptibility of traditional mode indices to forced mean-state changes, and forced changes in the MoV in a warming world. The sensitivity to model resolution is also explored using the newly available CESM1HR and CESM1SR ensembles. The CVDPv6 is unique in allowing users to account for changes in base state climate through various methods, and leverages the strengths of large ensembles in allowing for ensemble mean removal of the forced signal (Maher et al. 2025).

A number of important findings have been documented. These include the susceptibility of traditional MoV indices to base-state aliasing. In addition, robust forced changes have been demonstrated across all ensembles in both interannual variability generally (Figs. 2, 3) and in specific MoV. In some instances, future changes are similar across ensembles, such as for example the increase of T_{2m} variability over low latitude land regions (Fig. 2) and the intensification of interannual precipitation variability across the vast majority of the globe (Fig. 3). Various changes in some MoV are also shown to be shared across ensembles, such as the intensification of El Niño composite anomalies in T_{2m} over the Amazon and Northern Africa, and in P over the eastern equatorial Pacific Ocean. Patterns of future changes in AMV and NAO changes are also fairly consistent across models, with the mean PC with the multi-ensemble mean across ensembles greater than 0.5. However an equally notable finding is that, for most modes, structural uncertainties in projected patterns of change are large and, even in the case of consensus among SR models, patterns in CESM1HR often differ significantly from those in SR models, thus drawing attention to the important role played by model resolution in overall structural uncertainty. Consensus in simulated MoV changes across SR models does not on its own guarantee robustness. In addition, CESM1HR fails to outperform CESM1SR in its ability to reproduce observed MoV, as evidenced by its overall mean scores (0.83±0.00 versus 0.85±0.00 for CESM1SR) and reduced scores for multiple individual modes (Figs. 2 to 14, Table S4).

There are also various caveats to the current analysis that remain to be addressed. Foremost, there are important potential contributors to differences across ensembles that may not relate solely to model structure. These include differences in the scenarios used, which involve both contrasts in the 20th (i.e. CMIP5 vs CMIP6) and 21st centuries (RCP85 vs SSP370) and their specifications of greenhouse gases, sulfate aerosols, and other external forcing agents. The base-state warming and hydrologic changes of the models, particularly in the future period, also differ and these can drive contrasts in MoV across ensembles. The degree of independence between models, even between CESM and E3SM versions, also remains an open question as these models branched from a common model roughly a decade ago, potentially limiting the sampling of structural uncertainty explored here, though large changes in the models have occurred in recent years (Golaz et al., 2019, 2022, Danabasoglu et al. 2020). An additional uncertainty arises from the relatively limited 10-member ensemble sizes produced using CESM1SR and CESM1HR and there is no opportunity to assess structural contrasts across multiple HR/SR pairs for lack of model availability.

Finally, while model ensembles allow for isolation of variability no analogous approach exists using observations. By comparing the RMSE of MoV indices in individual members against indices derived when removing the EM, optimal methods can be explored. In the analysis of the ensembles used here, our results suggest that observational analyses are best conducted using linear fits for SLP-based modes, and either quadratic or 30-year running mean fits for temperature-based modes, in estimating and removing forced contributions.

Acknowledgements. This work was supported by the Regional and Global Model Analysis (RGMA) component of the Earth and Environmental System Modeling Program of the U.S. Department of Energy's Office of Biological and Environmental Research (BER) under Award DE-SC0022070. Development of the E3SM model is supported as part of the Energy Exascale Earth System Model (E3SM) project, funded by the U.S. Department of Energy, Office of Science, Office of Biological and Environmental Research. This work also was supported by the NSF National Center for Atmospheric Research, which is a major facility sponsored by the National Science Foundation (NSF) under Cooperative Agreement 1852977. The efforts of Dr. Fasullo in this work were supported by NASA Awards 80NSSC17K0565 and 80NSSC22K0046, and NSF Award 2103843. Computing resources were provided by the Climate Simulation Laboratory at NCAR's Computational and Information Systems Laboratory, sponsored by the National Science Foundation and other agencies. The CESM project is supported primarily by the National Science Foundation. This research used resources of the National Energy Research Scientific Computing Center (NERSC), a DOE Office of Science User Facility supported by the Office of Science of the U.S. Department of Energy under Contract DE-AC02- 05CH11231 using NERSC awards BER-ERCAP0020104 (E3SM2-LE-SSP370) and BER-ERCAP0025058 (E3SM1- LE). Lawrence Livermore National Laboratory is operated by Lawrence Livermore National Security, LLC, for the U.S. Department of Energy, National Nuclear Security Administration under Contract DE-AC52-07NA27344.

Data availability statement. The data for this study are available on the Earth System Grid (https://aims2.llnl.gov/search). The CVDPv6 output and analysis metrics of other modes presented in this study have also been made available via NCAR's Global Data Exchange (pending). Access to CERA20C can be found at https://apps.ecmwf.int/archive-catalogue/?class=ep and access to ERA-I can be found at https://apps.ecmwf.int/archive-catalogue/?class=ei. Access to ERA5 can be found at https://confluence.ecmwf.int/display/CKB/How+to+download+ERA5. Access to MERRA-2 is available at https://disc.gsfc.nasa.gov/datasets?project=MERRA-2. Access to GPCP data is at https://psl.noaa.gov/data/gridded/data.gpcp.html. Access to HadISST is at https://www.metoffce.gov.uk/hadobs/hadisst/ and to ERSSTv5 at https://psl.noaa.gov/data/gridded/data.noaa.ersst.v5.html. The GISTEMPv4 data are available at https://data.giss.nasa.gov/gistemp/ and the BEST data can be obtained at https://berkeleyearth.org/data/.

REFERENCES

Adler, R. F., Gu, G., Huffman, G. J., Sapiano, M. R., & Wang, J. J., 2020: GPCP and the Global Characteristics of Precipitation. *In Satellite Precipitation Measurement*: Volume **2** (pp. 677-697). Cham: Springer International Publishing.

Amaya, D. J. 2019:. The Pacific meridional mode and ENSO: *A review. Current Climate Change Reports*, **5**(4), 296-307, doi:10.1007/s40641-019-00142-x.

Arias, P. A. et al. Technical summary. In Climate Change 2021: The Physical Science Basis. Contribution of Working Group I to the Sixth Assessment Report of the Intergovernmental Panel on Climate Change (eds Masson–Delmotte, V. et al.) 33–144 (Cambridge Univ. Press, 2021).

Beobide-Arsuaga, G., Suarez-Gutierrez, L., Barkhordarian, A. et al, 2025: Increasing central and northern European summer heatwave intensity due to forced changes in internal variability. *Nat Commun,* **16**, 9485, https://doi.org/10.1038/s41467-025-65392-w

Branstator, G., and F. Selten, 2009: “Modes of variability” and Climate Change. *J. Climate*, **22**(10), 2639-2658.

Cai, W., Santoso, A., Wang, G., Yeh, S. W., An, S. I., Cobb, K. M., ... & Wu, L., 2015: ENSO and greenhouse warming. *Nature Climate Change*, **5**(9), 849-859, doi: 10.1038/nclimate2743.

Cai, W., Santoso, A., Wang, G., Wu, L., Collins, M., Lengaigne, M., ... & Timmermann, A., 2020: ENSO response to greenhouse forcing. El Niño Southern Oscillation in a changing Climate, 289-307, doi: 10.1002/9781119548164.ch13.

Cai, W., Yang, K., Wu, L., Huang, G., Santoso, A., Ng, B., ... & Yamagata, T., 2021: Opposite response of strong and moderate positive Indian Ocean Dipole to global warming. *Nature Climate Change*, **11**(1), 27-32, doi:10.1038/s41558-020-00943-1.

Chang, P., Zhang, S., Danabasoglu, G., Yeager, S. G., Fu, H., Wang, H., ... & Wu, L., 2020: An unprecedented set of high-resolution earth system simulations for understanding multiscale interactions in climate variability and change. *J Advances in Modeling Earth Systems*, **12**(12), doi: 10.1029/2020MS002298.

Chang, P., Fu, D., Liu, X., Castruccio, F. S., Prein, A. F., Danabasoglu, G., ... & Bates, S. C. 2025:. Future extreme precipitation amplified by intensified mesoscale moisture convergence. *Nature Geoscience*, **19**, doi: 10.1038/s41561-025-01859-1.

Chen, S., Chen, W., Xie, S. P., Yu, B., Wu, R., Wang, Z., ... & Graf, H. F., 2024: Strengthened impact of boreal winter North Pacific Oscillation on ENSO development in warming climate. *npj Climate and Atmospheric Science*, **7**(1), doi:10.1038/s41612-024-00615-3.

Chiang, J. C., & Vimont, D. J., 2004: Analogous Pacific and Atlantic meridional modes of tropical atmosphere–ocean variability. *J. Climate*, **17**(21), doi:10.1175/JCLI4953.1.

Dai, A. 2016: Future warming patterns linked to today's climate variability. *Scientific Reports*, **6**(1), 19110, doi:10.1038/srep19110.

Danabasoglu, G., Lamarque, J. F., Bacmeister, J., Bailey, D. A., DuVivier, A. K., Edwards, J., ... & Strand, W. G., 2020: The community earth system model version 2 (CESM2). *J Advances in Modeling Earth Systems*, **12**(2), doi:10.1029/2019MS001916.

Dee, D. P., Uppala, S., Simmons, A. J., Berrisford, P., Poli, P., Kobayashi, S., ... & Vitart, F. 2011: The ERA-Interim reanalysis: Configuration and performance of the data assimilation system. *Quarterly J the Royal Meteorological Society*, **137**(656), 553-597, doi:https://doi.org/10.1002/qj.828.

Delworth, T. L., & Zeng, F. 2016: The impact of the North Atlantic Oscillation on climate through its influence on the Atlantic meridional overturning circulation. *J. Climate*, **29**(3), 941-962, doi:10.1175/JCLI-D-15-0396.1.

Delworth, T. L., Zeng, F., Vecchi, G. A., Yang, X., Zhang, L., & Zhang, R. 2016: The North Atlantic Oscillation as a driver of rapid climate change in the Northern Hemisphere. *Nature Geoscience*, **9**(7), 509-512, doi:10.1038/ngeo2738.

Deser, C., M. A. Alexander, S. -P. Xie, and A. S. Phillips, 2010: Sea surface temperature variability: patterns and mechanisms. *Ann. Rev. Mar. Sci.*, **2010**.2, 115-143, doi:10.1146/annurev-marine-120408-151453.

Deser, C., A. S. Phillips, R. A. Tomas, Y. Okumura, M. A. Alexander, A. Capotondi, J. D. Scott, Y. -O. Kwon, and M. Ohba, 2012: ENSO and Pacific Decadal Variability in Community Climate System Model Version 4. *J. Climate*, **25**, 2622-2651, 10.1175/JCLI-D-11-00301.1

Deser, C., Hurrell, J. W., & Phillips, A. S., 2017: The role of the North Atlantic Oscillation in European climate projections. *Climate Dynamics*, **49**, 3141-3157, doi:10.1007/s00382-016-3502-z.

Deser, C., Lehner, F., Rodgers, K. B., Ault, T., Delworth, T. L., DiNezio, P. N., ... & Ting, M., 2020: Insights from Earth system model initial-condition large ensembles and future prospects. *Nature Climate Change*, **10**(4), 277-286, doi:10.1038/s41558-020-0731-2.

Deser, C., & Phillips, A. S., 2021: Defining the internal component of Atlantic multidecadal variability in a changing climate. *Geophysical Research Letters*, **48**(22), doi:10.1029/2021GL095023.

Deser, C. & Phillips, A. S., 2023: Spurious Indo-Pacific connections to internal Atlantic Multidecadal Variability introduced by the global temperature residual method. *Geophys. Res. Lett.*, **50**, doi: 10.1029/2022GL100574.

Deser, C., W. M. Kim, R. C. J. Wills, I. R. Simpson, S. Yeager, G. Danabasoglu, K. Rodgers and N. Rosenbloom, 2024: Effects of macro vs. micro initialization and ocean initial-condition memory on the evolution of ensemble spread in the CESM2 Large Ensemble. *Clim. Dyn.*, **63**, doi: 10.1007/s00382-024-07553-z.

Di Lorenzo, E., Xu, T., Zhao, Y., Newman, M., Capotondi, A., Stevenson, S., ... & Zhang, H. 2023: Modes and mechanisms of Pacific decadal-scale variability. *Annual Review of Marine Science*, **15**(1), 249-275, doi:10.1146/annurev-marine-040422-084555.

Eyring, V., Bony, S., Meehl, G. A., Senior, C. A., Stevens, B., Stouffer, R. J., & Taylor, K. E., 2016: Overview of the Coupled Model Intercomparison Project Phase 6 (CMIP6) experimental design and organization. *Geoscientific Model Development*, **9**(5), 1937-1958, doi:10.5194/gmd-9-1937-2016.

Fasullo, J. T., Otto-Bliesner, B. L., & Stevenson, S., 2018: ENSO's changing influence on temperature, precipitation, and wildfire in a warming climate. *Geophysical Research Letters*, **45**(17), 9216-9225, doi:10.1029/2018GL079022.

Fasullo, J. T., Phillips, A. S., & Deser, C., 2020: Evaluation of leading modes of climate variability in the CMIP archives. *J Climate*, **33**(13), 5527-5545, doi:10.1175/JCLI-D-19-1024.1.

Fasullo, J.T., Lamarque, J. F., Hannay, C., Rosenbloom, N., Tilmes, S., DeRepentigny, P., ... & Deser, C 2022: Spurious Late Historical-Era Warming in CESM2 Driven by Prescribed Biomass Burning Emissions, *Geo. Res. Lett.*, **49**, doi:10.1029/2021GL097420.

Fasullo, J. T., Caron, J. M., Phillips, A., Li, H., Richter, J. H., Neale, R. B., ... & Arblaster, J. 2024: Modes of Variability in E3SM and CESM Large Ensembles. *J Climate*, **37**(8), 2629-2653, doi:10.1175/JCLI-D-23-0454.1.

Fogt, R. L., & Marshall, G. J. 2020:. The Southern Annular Mode: variability, trends, and climate impacts across the Southern Hemisphere. *Wiley Interdisciplinary Reviews: Climate Change*, **11**(4), https://doi.org/10.1002/wcc.652.

Forster, P. M., Andrews, T., Good, P., Gregory, J. M., Jackson, L. S., & Zelinka, M. 2013:. Evaluating adjusted forcing and model spread for historical and future scenarios in the CMIP5 generation of climate models. *J Geophysical Research: Atmospheres*, **118**(3), 1139-1150, doi:10.1002/jgrd.50174.

Fuentes-Franco, R., Docquier, D., Koenigk, T., Zimmermann, K., & Giorgi, F. 2023:. Winter heavy precipitation events over Northern Europe modulated by a weaker NAO variability by the end of the 21st century. *Npj Climate and Atmospheric Science*, **6**(1), 72, doi:10.1038/s41612-023-00396-1.

Fyfe, J. C., Kharin, V. V., Santer, B. D., Cole, J. N. S., and Gillett,N. P. 2021: Significant impact of forcing uncertainty in a large ensemble of climate model simulations, *P. Natl. Acad. Sci.* USA, **118**, e2016549118, https://doi.org/10.1073/pnas.2016549118.

Gettelman, A., Hannay, C., Bacmeister, J. T., Neale, R. B., Pendergrass, A. G., Danabasoglu, G., ... & Mills, M. J. 2019:. High climate sensitivity in the Community Earth System Model version 2 (CESM2). *Geophysical Research Letters*, **46**(14), 8329-8337, doi: 10.1029/2019GL083978.

Golaz, Jean-Christophe, Peter M. Caldwell, Luke P. Van Roekel, Mark R. Petersen, Qi Tang, Jonathan D. Wolfe, Guta Abeshu et al. 2019: The DOE E3SM coupled model version 1: Overview and evaluation at standard resolution. *J Advances in Modeling Earth Systems*, **11**(7), 2089-2129, doi:10.1029/2018MS001603.

Golaz, J. C., Van Roekel, L. P., Zheng, X., Roberts, A. F., Wolfe, J. D., Lin, W., … & Bader, D. C. 2022:. The DOE E3SM model version 2: Overview of the physical model and initial model evaluation. *J Advances in Modeling Earth Systems*, **14**(12), doi:10.1029/2022MS003156.

Guinaldo, T., Cassou, C., Sallée, J. B., & Liné, A. 2025:. Internal variability effect doped by climate change drove the 2023 marine heat extreme in the North Atlantic. Communications Earth & Environment, **6**(1), 291, doi:10.1038/s43247-025-01367-5.

Hamouda, M. E., Pasquero, C., & Tziperman, E. 2021: Decoupling of the Arctic Oscillation and North Atlantic Oscillation in a warmer climate. *Nature Climate Change*, **11**(2), 137-142, doi:10.1038/s41558-020-00916-8.

Haszpra, T., Herein, M., & Bódai, T. 2020:. Investigating ENSO and its teleconnections under climate change in an ensemble view–a new perspective. *Earth System Dynamics*, **11**(1), 267-280, doi:10.5194/esd-11-267-2020.

He, C., & Li, T. 2019:. Does global warming amplify interannual climate variability?. *Climate Dynamics*, **52**(5), 2667-2684, doi:10.1007/s00382-018-4289-9.

Hersbach, H., Bell, B., Berrisford, P., Hirahara, S., Horányi, A., Muñoz-Sabater, J., ... & Thépaut, J. N. (2020). The ERA5 global reanalysis. Quarterly journal of the royal meteorological society, 146(730), 1999-2049, doi:doi.org/10.1002/qj.3803.

Holland, M. M., Hannay, C., Fasullo, J., Jahn, A., Kay, J. E., Mills, M., … & Bailey, D. 2024:. New model ensemble reveals how forcing uncertainty and model structure alter climate simulated across CMIP generations of the Community Earth System Model. *Geoscientific Model Development*, **17**(4), 1585-1602, doi:10.5194/gmd-17-1585-2024.

Hu, Z. Z., McPhaden, M. J., Huang, B., Zhu, J., & Liu, Y. 2024:. Accelerated warming in the North Pacific since 2013. *Nature Climate Change*, **14**(9), 929-931, doi:10.1038/s41558-024-02040-y.

Hurrell, J. W., & Deser, C. (2010). North Atlantic climate variability: the role of the North Atlantic Oscillation. J Marine Systems, 79(3-4), 231-244, doi:10.1016/j.jmarsys.2009.11.002.

Iles, C., & Hegerl, G. 2017:. Role of the North Atlantic Oscillation in decadal temperature trends. *Environmental Research Letters*, **12**(11), 114010, doi:10.1088/1748-9326/aa9152.

Ji, K., Yu, J. Y., Li, J., Hu, Z. Z., Tseng, Y. H., Shi, J., … & Ding, R. 2024:. Enhanced North Pacific Victoria mode in a warming climate. *npj Climate and Atmospheric Science*, **7**(1), 49, doi:10.1038/s41612-024-00600-1.

Jia, F., Cai, W., Geng, T., Gan, B., Zhong, W., Wu, L., & McPhaden, M. J. 2025:. Transition from multi-year La Niña to strong El Niño rare but increased under global warming. *Science Bulletin*, **70**(5), 756-764, doi:10.1016/j.scib.2024.12.034.

Kay, J. E., Deser, C., Phillips, A., Mai, A., Hannay, C., Strand, G., … & Vertenstein, M. 2015:. The Community Earth System Model (CESM) large ensemble project: A community resource for studying climate change in the presence of internal climate variability. *Bulletin of the American Meteorological Society*, **96**(8), 1333-1349, doi:10.1175/BAMS-D-13-00255.1.

Kim, S. K., Park, H. J., An, S. I., Liu, C., Cai, W., Santoso, A., & Kug, J. S. 2024:. Decreased Indian Ocean Dipole variability under prolonged greenhouse warming. *Nature Communications*, **15**(1), 2811, doi:10.1038/s41467-024-47276-7.

Knutti, R., Sedláček, J., Sanderson, B. M., Lorenz, R., Fischer, E. M., & Eyring, V. 2017:. A climate model projection weighting scheme accounting for performance and interdependence. *Geophysical Research Letters*, **44**(4), 1909-1918, doi:10.1002/2016GL072012.

Kostov, Y., Marshall, J., Hausmann, U., Armour, K. C., Ferreira, D., & Holland, M. M. 2017:. Fast and slow responses of Southern Ocean sea surface temperature to SAM in coupled climate models. *Climate Dynamics*, **48**, 1595-1609, doi:10.1007/s00382-016-3162-z.

Lee, J., K. Sperber, P. Gleckler, K. Taylor, and C. Bonfils, 2021: Benchmarking performance changes in the simulation of extratropical modes of variability across CMIP generations. *J Climate*, **34**, 6945–6969, doi:10.1175/JCLI-D-20-0832.1.

Liang, Y., Gillett, N. P., & Monahan, A. H. 2024:. Accounting for Pacific climate variability increases projected global warming. *Nature Climate Change*, **14**(6), 608-614, doi:10.1038/s41558-024-01933-2.

Liu, Z., & Di Lorenzo, E. 2018:. Mechanisms and predictability of Pacific decadal variability. *Current Climate Change Reports*, **4**, 128-144, doi:10.1007/s40641-018-0090-5.

Maher, N., Matei, D., Milinski, S., & Marotzke, J. 2018:. ENSO change in climate projections: Forced response or internal variability? *Geophysical Research Letters*, **45**, 11,390–11,398. https://doi.org/10.1029/2018GL079764.

Maher, N., Phillips, A. S., Deser, C., Wills, R. C. J., Lehner, F., Fasullo, J., ... & Beyerle, U. 2025: The updated Multi-Model Large Ensemble Archive and the Climate Variability Diagnostics Package: New tools for the study of climate variability and change. *Geo. Model Dev*., doi:10.5194/gmd-18-6341-2025.

Mantua, N. J., & Hare, S. R. 2002: The Pacific decadal oscillation. *J Oceanography*, **58**(1), 35-44, doi:10.1023/A:1015820616384.

McGregor, G. 2024:. Modes of Climate Variability. In Heatwaves: Causes, Consequences and Responses (pp. 169-206). Cham: Springer International Publishing, doi:10.1007/978-3-031-69906-1_8.

McPhaden, M. J., Lee, T., Fournier, S., & Balmaseda, M. A. 2020: ENSO observations. El Niño Southern Oscillation in a Changing Climate, 39-63, doi:10.1002/9781119548164.ch3.

Meinshausen, M., Smith, S. J., Calvin, K., Daniel, J. S., Kainuma, M. L., Lamarque, J. F., ... & Van Vuuren, D. P. P. 2011:. The RCP greenhouse gas concentrations and their extensions from 1765 to 2300. *Climatic Change*, **109**(1), 213, doi:10.1007/s10584-011-0156-z.

Ng, B., Cai, W., Cowan, T., & Bi, D. 2018:. Influence of internal climate variability on Indian Ocean Dipole properties. *Scientific Reports*, **8**(1), 13500, doi:10.1038/s41598-018-31842-3.

O'Brien, J. P. and C. Deser, 2023: Quantifying and understanding forced changes to unforced modes of atmospheric circulation variability over the North Pacific in a coupled model large ensemble. *J. Climate*, **36**, 17-35, doi: 10.1175/JCLI-D-22-0101.1.

Polonsky, A., & Torbinsky, A. 2021: The IOD–ENSO interaction: The Role of the Indian Ocean Current's system. *Atmosphere*, **12**(12), 1662, doi:10.3390/atmos12121662.

Power, S., Lengaigne, M., Capotondi, A., Khodri, M., Vialard, J., Jebri, B., ... & Henley, B. J. 2021:. Decadal climate variability in the tropical Pacific: Characteristics, causes, predictability, and prospects. *Science*, **374**(6563), doi:10.1126/science.aay9165.

Rodgers, K. B., Lee, S. S., Rosenbloom, N., Timmermann, A., Danabasoglu, G., Deser, C., ... & Yeager, S. G. 2021:. Ubiquity of human-induced changes in climate variability. *Earth System Dynamics*, **12**(4), 1393-1411, doi:10.5194/esd-12-1393-2021.

Saji N.H., Goswami B.N., Vinayachandran P.N., Yamagata T., 1999: A dipole mode in the tropical Indian Ocean, *Nature*, **401**, 360-363, doi:10.1038/43854.

Seager, R., Osborn, T. J., Kushnir, Y., Simpson, I. R., Nakamura, J., & Liu, H. 2019:. Climate variability and change of Mediterranean-type climates. *J Climate*, **32**(10), 2887-2915, doi:10.1175/JCLI-D-18-0472.1.

Son, S. W., & Lee, S. (2006). Preferred modes of variability and their relationship with climate change. *J Climate*, **19**(10), 2063-2075, doi:10.1175/JCLI3823.1.

Stevenson, S., Huang, X., Zhao, Y., Di Lorenzo, E., Newman, M., van Roekel, L., ... & Capotondi, A. 2023:. Ensemble spread behavior in coupled climate models: Insights from the Energy Exascale Earth System Model version 1 large ensemble. *J Advances in Modeling Earth Systems*, **15**(7), doi:10.1029/2023MS003653.

Stuecker, M. F., Zhao, S., Timmermann, A., Ghosh, R., Semmler, T., Lee, S. S., ... & Jung, T. 2025:. Global climate mode resonance due to rapidly intensifying El Niño-Southern Oscillation. *Nature Communications*, **16**(1), 9013, doi: 10.1038/s41467-025-64619-0.

Suarez-Gutierrez, L. & Maher, N. (2026). Temperature variability projections remain uncertain after constraining them to best performing Large Ensembles of individual Climate Models. *Nature Communications*, doi: 10.1038/s41467-025-67005-y.

Sun, S., Fang, Y., Zu, Y., Liu, L., & Li, K. 2022:. Increased occurrences of early Indian Ocean Dipole under global warming. *Science Advances*, **8**(47), doi:10.1126/sciadv.add6025.

Thompson, D. W., & Wallace, J. M. (2000). Annular modes in the extratropical circulation. Part I: Month-to-month variability. *J Climate*, **13**(5), 1000-1016, doi:10.1175/1520-0442(2000)013<1000:AMITEC>2.0.CO;2.

Thornton, P. K., Ericksen, P. J., Herrero, M., & Challinor, A. J. 2014:. Climate variability and vulnerability to climate change: a review. *Global Change Biology*, **20**(11), 3313-3328, doi:10.1111/gcb.12581.

Van Oldenborgh, G. J., van Der Wiel, K., Kew, S., Philip, S., Otto, F., Vautard, R., ... & van Aalst, M. 2021:. Pathways and pitfalls in extreme event attribution. *Climatic Change*, **166**(1), 13, doi:10.1007/s10584-021-03071-7.

Vázquez, D. P., Gianoli, E., Morris, W. F., & Bozinovic, F. 2017:. Ecological and evolutionary impacts of changing climatic variability. *Biological Reviews*, **92**(1), 22-42, doi:10.1111/brv.12216.

Wang, G., Cai, W., Gan, B., Wu, L., Santoso, A., Lin, X., ... & McPhaden, M. J. 2017:. Continued increase of extreme El Niño frequency long after 1.5 C warming stabilization. *Nature Climate Change*, **7**(8), 568-572, doi:10.1038/nclimate3351.

Wang, Y., Luo, Y., Lu, J., & Liu, F. 2019:. Changes in ENSO amplitude under climate warming and cooling. *Climate Dynamics*, **52**, 1871-1882, doi:10.1007/s00382-018-4225-5.

Wang, B., Sun, W., Jin, C., Luo, X., Yang, Y. M., Li, T., ... & Liu, J. 2023:. Understanding the recent increase in multiyear La Niñas. *Nature Climate Change*, **13**(10), 1075-1081, doi:10.1038/s41558-023-01830-9.

Wang, G., Cai, W., Santoso, A., Abram, N., Ng, B., Yang, K., ... & Li, X. 2024:. The Indian Ocean Dipole in a warming world. *Nature Reviews Earth & Environment*, **5**(8), 588-604, doi:10.1038/s43017-024-00662-2.

Wengel, C., Lee, S. S., Stuecker, M. F., Timmermann, A., Chu, J. E., & Schloesser, F. 2021:. Future high-resolution El Niño/Southern oscillation dynamics. *Nature Climate Change*, 11(9), 758-765, doi:10.1038/s41558-021-01130-0.

Wills, R. C., Herrington, A. R., Simpson, I. R., & Battisti, D. S. 2024:. Resolving weather fronts increases the large-scale circulation response to Gulf Stream SST anomalies in variable-resolution CESM2 simulations. *J Advances in Modeling Earth Systems*, **16**(7), doi:10.1029/2023MS004123.

Woollings, T., Barriopedro, D., Methven, J., Son, S. W., Martius, O., Harvey, B., ... & Seneviratne, S. 2018:. Blocking and its response to climate change. Current climate change reports, 4, 287-300, doi:10.1007/s40641-018-0108-z.

Yang, Y., Wu, L., Guo, Y., Gan, B., Cai, W., Huang, G., ... & Xie, S. P. 2021:. Greenhouse warming intensifies north tropical Atlantic climate variability. *Science Advances*, **7**(35), doi:10.1126/sciadv.abg9690.

Zheng, X. T., Lu, J., & Hui, C. 2021:. Response of seasonal phase locking of Indian Ocean Dipole to global warming. *Climate Dynamics*, **57**(9), 2737-2751, doi:10.1007/s00382-021-05824-3.